HHS Public Access

Author manuscript

Immunity. Author manuscript; available in PMC 2024 January 30.

Published in final edited form as:

Immunity. 2022 February 08; 55(2): 308–323.e9. doi:10.1016/j.immuni.2021.10.020.

Type I interferon activates MHC class I-dressed CD11b^{+} conventional dendritic cells to promote protective anti-tumor CD8^{+} T cell immunity

Ellen Duong[1,2], **Tim B. Fessenden**[1], **Emi Lutz**[1,3], **Teresa Dinter**[1,2], **Leon Yim**[1], **Sarah Blatt**[1], **Arjun Bhutkar**[1], **Karl Dane Wittrup**[1,3], **Stefani Spranger**[1,2,4,5,*]

[1]Koch Institute for Integrative Cancer Research at MIT, Cambridge, MA, USA

[2]Department of Biology, MIT, Cambridge, MA, USA

[3]Department of Biological Engineering, MIT, Cambridge, MA, USA

[4]Ragon Institute of MGH, MIT and Harvard, Cambridge, MA, USA

[5]Lead contact

SUMMARY

Tumor-infiltrating dendritic cells (DCs) assume varied functional states that impact anti-tumor immunity. To delineate the DC states associated with productive anti-tumor T cell immunity, we compared spontaneously regressing and progressing tumors. Tumor-reactive CD8^{+} T cell responses in *Batf3*$^{-/-}$ mice lacking type 1 DCs (DC1s) were lost in progressor tumors but preserved in regressor tumors. Transcriptional profiling of intra-tumoral DCs within regressor tumors revealed an activation state of CD11b^{+} conventional DCs (DC2s) characterized by expression of interferon (IFN)-stimulated genes (ISGs) (ISG^{+} DCs). ISG^{+} DC-activated CD8^{+} T cells *ex vivo* comparably to DC1. Unlike cross-presenting DC1, ISG^{+} DCs acquired and presented intact tumor-derived peptide-major histocompatibility complex class I (MHC class I) complexes. Constitutive type I IFN production by regressor tumors drove the ISG^{+} DC state, and activation of MHC class I-dressed ISG^{+} DCs by exogenous IFN-β rescued anti-tumor immunity against progressor tumors in *Batf3*$^{-/-}$ mice. The ISG^{+} DC gene signature is detectable in human tumors. Engaging this functional DC state may present an approach for the treatment of human disease.

In brief

*Correspondence: spranger@mit.edu.

AUTHOR CONTRIBUTIONS

E.D. and S.S. conceptualized the study, designed experiments, and interpreted data. E.D. performed experiments, analyzed data, and wrote the manuscript. T.B.F. generated CRISPR-modified cell lines. T.B.F. and E.D. performed image analyses. E.L. generated recombinant IFN-β proteins. T.D. and L.Y. performed human and mouse tumor line screens and assisted with experiments. A.B., S.B., and E.D. performed computational analyses. E.D., T.B.F., T.D., E.L., and S.S. reviewed and edited the manuscript. S.S. acquired funding and supervised the study.

DECLARATION OF INTERESTS

The authors declare no competing interests. Part of this work contributed to the US patent 17/348,704 with E.D. and S.S. as inventors. S.S. is a co-founder of Danger Bio and a consultant or SAB member of Arcus Biosciences, Dragonfly Therapeutics, TAKEDA, Merck, Ribon Therapeutics, and Tango Therapeutics. These activities are not in conflict with the presented data.

SUPPLEMENTAL INFORMATION

Supplemental information can be found online at https://doi.org/10.1016/j.immuni.2021.10.020.

Tumor-infiltrating dendritic cells (DCs) are central to the anti-tumor immune response. Duong et al. reveal an activation state of CD11b$^+$ conventional DCs (DC2) characterized by expression of interferon (IFN)-stimulated genes (ISG$^+$ DCs) and capable of acquiring and presenting intact tumor-derived peptide-MHC class I complexes. ISG$^+$ DCs can activate CD8$^+$ T cells and promote protective anti-tumor immunity in the absence of DC1.

Graphical Abstract

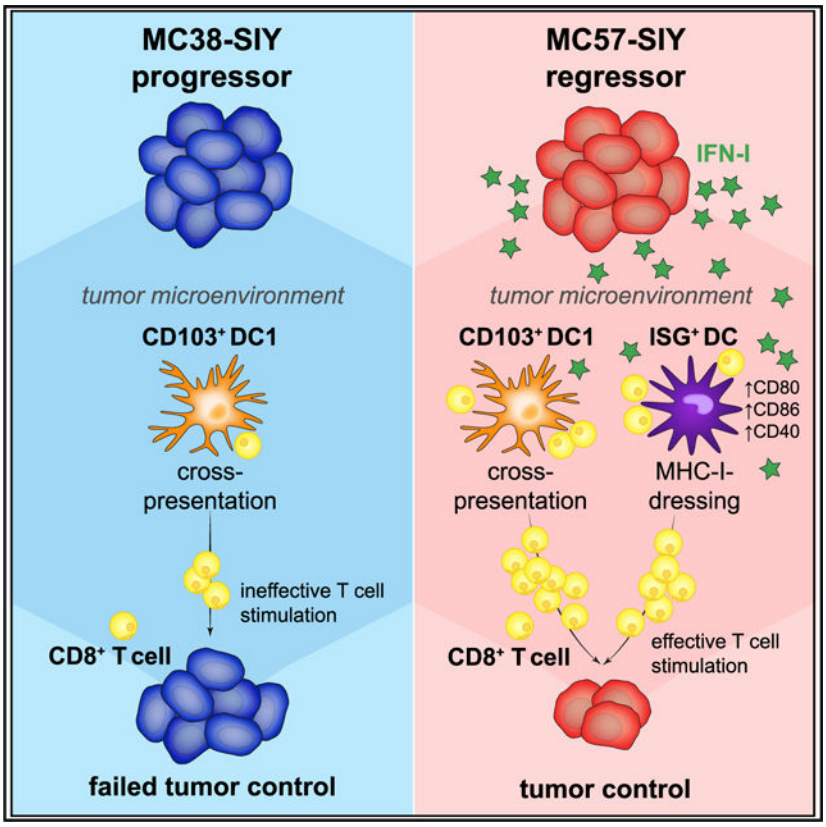

INTRODUCTION

Cytotoxic CD8$^+$ T cell responses are critical for potent anti-tumor immunity (Fridman et al., 2012). The generation of tumor-specific CD8$^+$ T cells (priming) occurs in the tumor-draining lymph node (tdLN) through interactions of naive T cells with dendritic cells (DCs) (Chen and Mellman, 2013). During these interactions, DCs present tumor antigens on major histocompatibility complex class I (MHC class I) and provide costimulation and cytokine signaling (Inaba et al., 1987).

The DC compartment is heterogeneous but has been defined as comprising conventional DCs (cDCs) and plasmacytoid DCs (pDCs). cDCs can be further subdivided into two populations, CD8α$^+$/CD103$^+$ DC1s and CD11b$^+$/Sirpα$^+$ DC2s, with distinct developmental requirements and functional specialization (Eisenbarth, 2019; Guilliams et al., 2014, 2016; Merad et al., 2013; Mildner and Jung, 2014; Murphy et al., 2016). DC1s require the

transcription factors IRF8 and Batf3 for development and are adept at cross-presenting cell-associated antigens to $CD8^+$ T cells (den Haan et al., 2000; Edelson et al., 2010; Hildner et al., 2008; Iyoda et al., 2002; Schulz and Reis e Sousa, 2002; Tamura et al., 2005). In contrast, DC2s are driven by IRF4 and are more potent at stimulating $CD4^+$ T cells (Gao et al., 2013; Krishnaswamy et al., 2017; Tamura et al., 2005; Tussiwand et al., 2015; Williams et al., 2013). The inclusion of monocytes that are recruited to inflammatory sites and differentiate into DC-like cells (moDCs) has further increased the diversity of the DC compartment (Briseño et al., 2016; León et al., 2007; Menezes et al., 2016; Serbina et al., 2003).

Recent studies indicate that these DC subsets are generally conserved across species (Gerhard et al., 2021; Zilionis et al., 2019) and can be found in solid tumors (Broz et al., 2014; Laoui et al., 2016). Different tumor types harbor distinct compositions of DCs (Laoui et al., 2016) that can impact the resultant anti-tumor T cell response. In murine tumor models, DC1s are regarded as the most critical DC subset driving anti-tumor immunity given their specialized ability to cross-present antigens (Broz et al., 2014; Hildner et al., 2008; Roberts et al., 2016). Accordingly, tumors with a greater DC1 infiltrate tend to be better controlled (Salmon et al., 2016; Spranger et al., 2015), and the presence of the DC1 signature in patient tumors is associated with the response to immunotherapy (Barry et al., 2018; Böttcher et al., 2018; Broz et al., 2014; Michea et al., 2018).

However, there is increasing evidence that tumor-infiltrating DCs can exist in distinct functional states with tremendous implications for the anti-tumor immune response. It was recently reported that activated DC1s in lung tumors (mregDCs) expressed an immunoregulatory program that dampened their ability to activate T cells (Maier et al., 2020). While progress has been made in understanding the role and function of DC1s, the contributions of other DCs to anti-tumor immunity remain poorly described. Notably, some reports demonstrate that under specific therapeutic settings, DC subsets distinct from DC1s can become robust $CD8^+$ T cell activators (Ma et al., 2013; Sharma et al., 2018). These studies point to the untapped potential of the DC compartment that can be harnessed to enhance anti-tumor T cell immunity and calls for more nuanced investigation into the functional DC states driving anti-tumor immunity.

In this study, we aimed to dissect the contributions of distinct DC states and their influence on anti-tumor T cell responses during a productive or dysfunctional anti-tumor immune response. By comparing the DC compartment of a spontaneously regressing tumor and a progressing tumor, we identified an activation state of $CD11b^+$ cDCs expressing an interferon (IFN)-stimulated gene (ISG) signature (ISG^+ DCs) that was enriched in regressor tumors. Similar to DC1s, ISG^+ DCs shared the ability to robustly activate $CD8^+$ T cells. However, while DC1s cross-presented antigens, ISG^+ DCs acquired and presented intact tumor-derived peptide (p)MHC class I complexes via MHC class I dressing. ISG^+ DCs were activated by local tumor cell-derived type I IFN (IFN-I) and could drive protective, systemic anti-tumor $CD8^+$ T cell immunity in mice lacking DC1s.

RESULTS

The regression of MC57-SIY tumors is independent of Batf3-driven DC1s

To identify functionally relevant DC states associated with productive anti-tumor immune responses, we established a comparative model system of a spontaneously regressing tumor (MC57-SIY fibrosarcoma) and a progressively growing tumor (MC38-SIY colon carcinoma) (Figure 1A), both expressing the model antigen SIYRYYGL (SIY).

Our initial analysis focused on the cDC compartment given its reported impact on anti-tumor immunity (Broz et al., 2014; Roberts et al., 2016; Spranger et al., 2015, 2017). At day 7 after tumor inoculation, we detected a greater proportion of $CD103^+$ DC1s in MC57-SIY tumors, whereas the DC compartment was skewed toward $CD11b^+$ DC2s in MC38-SIY tumors (Figures 1B and 1C). This phenotype was conserved in *Rag2*$^{-/-}$ mice, suggesting that T cells had a minimal impact on DC composition (Figures 1D–1F). A time course demonstrated that both DC1s and $CD8^+$ T cells accumulated in MC57-SIY tumors but not in MC38-SIY tumors (Figure S1A). Although recent studies highlighted a role for natural killer (NK) cells in DC1 recruitment (Barry et al., 2018; Böttcher et al., 2018), antibody-mediated depletion of NK cells in wild-type (WT) mice had no effect on the numbers of DC1s that infiltrated the tumors (Figure S1B) or on the regression of MC57-SIY tumors (Figure S1C).

To determine whether DC1s were necessary for tumor rejection, we implanted both cell lines into *Batf3*$^{-/-}$ mice lacking DC1s (Hildner et al., 2008). Consistent with published data (Broz et al., 2014; Hildner et al., 2008), growth of MC38-SIY tumors in *Batf3*$^{-/-}$ mice was accelerated compared to WT mice (Figure 1G). In contrast, MC57-SIY tumors were rejected in *Batf3*$^{-/-}$ mice with similar kinetics as in WT mice (Figure 1G), suggesting that regression was independent of DC1s. This notion was supported by the observation that only MC57-SIY tumors harbored SIY-specific and granzyme B-expressing T cells (Figures 1H and S1D–S1G). Furthermore, while systemic anti-tumor T cell responses against MC38-SIY tumors were completely ablated in *Batf3*$^{-/-}$ mice (Figure 1I), those against MC57-SIY tumors were preserved in *Batf3*$^{-/-}$ mice but reduced by 58% when compared to responses in WT mice (Figure 1I). These data indicate that DC1s are not the sole drivers of anti-tumor $CD8^+$ T cell responses in MC57-SIY tumors.

DC1s selectively express Clec9a, and signaling through this receptor promotes the cross-presentation of dead cell-associated antigens (Sancho et al., 2008, 2009; Zelenay et al., 2012; Zhang et al., 2012). Using *Clec9a*$^{-/-}$ mice, we affirmed that Clec9a-mediated cross-presentation by DC1s is not required for the rejection of MC57-SIY tumors (Figure S1H). One possibility bypassing the need for cross-presentation is tumor control by $CD4^+$ T cells (Mumberg et al., 1999). To assess whether regression of MC57-SIY is dependent on $CD8^+$ or $CD4^+$ T cells, we depleted each T cell subset alone or in combination and identified that tumor control was driven by $CD8^+$ T cells (Figure S1I). These data indicate that cross-priming of $CD8^+$ T cells is an essential component of anti-tumor immunity but that in certain contexts it can be induced independent of cross-presenting DC1s.

Functional assays and scRNA-seq identify a DC cluster characterized by an IFN-I gene signature in MC57-SIY tumors

We next aimed to identify the antigen-presenting cell (APC) type(s) mediating the induction of protective immunity against MC57-SIY tumors in *Batf3*$^{-/-}$ mice. We established a functional *ex vivo* co-culture assay using naive SIY-reactive 2C T cell receptor (TCR) transgenic T cells (Figure 2A). Myeloid APCs were sorted from MC57-SIY tumors in WT and *Batf3*$^{-/-}$ mice and co-cultured with dye-labeled 2C T cells. In this assay, T cell activation was solely dependent on spontaneous antigen presentation by APCs *in vivo*, as no exogenous SIY peptide was added. In both WT and *Batf3*$^{-/-}$ settings, only CD11c^{+} DCs, but not Ly6C^{+} monocytes or F4/80^{+} macrophages, were able to induce 2C T cell proliferation (Figures 2B and 2C). In the *Batf3*$^{-/-}$ setting, this implied the presence of stimulatory DCs in the tumor that were distinct from DC1s. To confirm the requirement of CD11c^{+} DCs for control of MC57-SIY tumors, we generated *Itgax*-diphtheria toxin receptor bone marrow chimeras (*Itgax-DTR* BMCs), a model where all CD11c^{+} (encoded by *Itgax*) cells expressed DTRs. Specific depletion of CD11c^{+} cells via DT administration completely abrogated anti-tumor CD8^{+} T cell responses against MC57-SIY tumors (Figure 2D), which confirmed an absolute requirement for CD11c^{+} DCs for anti-tumor immunity. To definitively confirm that bona fide DCs are required for anti-tumor immunity against MC57-SIY tumors, we also evaluated the immune response in zDC-DTR BMCs, a mouse model where only Zbtb46-dependent cDCs expressed DTRs (Meredith et al., 2012). Consistent with our observations in *Itgax-DTR* BMCs, selective depletion of cDCs completely ablated functional tumor-reactive T cell responses against MC57-SIY tumors (Figures 2E, S2A, and S2B). Collectively, these data provided a strong rationale for narrowing our search for stimulatory cells within the intratumoral DC compartment.

To identify the relevant DC states driving anti-tumor immunity, we performed single-cell RNA-sequencing (scRNA-seq) of the CD45^{+} immune infiltrate of regressor MC57-SIY tumors in *Rag2*$^{-/-}$ mice. The use of *Rag2*$^{-/-}$ mice improved cell yield, as MC57-SIY tumors could grow progressively in these mice. Based on expression of a canonical DC signature (*H2-Ab1*, *Flt3*, *Itgax*) (Figure 2F) and absence of marker genes corresponding to other lineages (Figure S2C; Table S1), we identified a global DC cluster that was computationally isolated and further subclustered (Figure S2D). We detected a contaminating macrophage cluster that was excluded from a second round of filtering (Figures S2D and S2E). These analyses led to the identification of seven distinct DC clusters (Figures 2F and 2G). By mapping the differentially expressed genes (DEGs) of each DC cluster to the literature (Guilliams et al., 2016; Merad et al., 2013; Mildner and Jung, 2014; Murphy et al., 2016; Zilionis et al., 2019), we identified several classically described subsets: DC1s, migratory DCs, DC2s, moDCs, and two distinct pDC clusters (Figure 2G; Table S2). To validate these assigned cluster identities, we scored the cells in our dataset for their expression of published DC subset-specific signatures and found that our assignments agreed with the published signatures (Table S3; Figure S2F) (Zilionis et al., 2019). Intriguingly, our DEG analysis identified one cluster, c2, that was enriched in ISGs for which we did not observe a comparable counterpart in the published DC signatures, although some cells in this cluster expressed a DC2 signature (Figure S2F). Based on its ISG expression, c2 likely represents an IFN-induced activation state, and we refer to this cluster as ISG^{+} DCs. Of note, a recent

study identified an inflammatory cDC2 state (Inf-cDC2s) that was induced by IFN-I during viral infection (Bosteels et al., 2020), and the Inf-cDC2 signature (generated in-house) was enriched in the ISG$^+$ DC cluster (Figures S2G and S2H; Table S3). The similarity in their transcriptional profiles might suggest that ISG$^+$ DCs and Inf-cDC2s are related activation states; however, direct comparative studies are needed to confirm this notion.

To determine whether induction of the ISG$^+$ DC state was required for anti-tumor immunity against our regressor model, we implanted MC57-SIY cells into *Ifnar1*$^{-/-}$ mice, wherein host cells are deficient in IFN-I sensing. We observed failed tumor control (Figure 2H), as well as reduced tumor-reactive T cell responses by IFN-γ enzyme-linked immunospot (ELISpot) (Figure S2I), thus confirming the necessity of host IFNAR signaling for anti-tumor immunity. Previous studies have shown that T cell activation can be impacted by defects in T cell-intrinsic IFN-I sensing (Hervas-Stubbs et al., 2011; Huber and Farrar, 2011). To determine whether IFN-I sensing is specifically required in the CD11c$^+$ DC compartment, we generated *Itgax-DTR:Ifnar1*$^{-/-}$ mixed BMCs using WT or *Ifnar1*$^{-/-}$ hosts (Figure 2I). DT administration in this model specifically ablated IFN-I sensing in the CD11c$^+$ DC compartment, while other immune compartments were unperturbed. We observed significant reductions in the systemic anti-tumor T cell response when DCs lacked the ability to sense IFN-I (Figure 2J). These data indicate that DC-intrinsic IFN-I sensing is required for induction of a potent anti-tumor T cell response, thus confirming a role for the ISG$^+$ DC state in anti-tumor immunity.

ISG$^+$ DCs are present in *Batf3*$^{-/-}$ mice and comprise an activation state of CD11b$^+$ DCs

To study the ISG$^+$ DCs, we identified *Axl* (Schmid et al., 2016) as a surface-expressed marker that differentiated the ISG$^+$ DC cluster from other DC clusters (Figure 3A; Table S4). As the ISG$^+$ DC cluster also expressed *Itgam* encoding CD11b (Figure 3A), we used the co-expression of AXL and CD11b to identify ISG$^+$ DCs. Given that AXL can be expressed on other immune cell types, we took measures in our gating strategy to ensure a specific analysis of DCs (Figures 3B, 3C, and S3A). This gating strategy enabled us to detect the presence of ISG$^+$ DCs in MC57-SIY tumors in WT and *Rag2*$^{-/-}$ mice, and, importantly, in *Batf3*$^{-/-}$ mice (Figures 3B–3I and S3A).

As ISG$^+$ DCs were originally identified in MC57-SIY tumors from *Rag2*$^{-/-}$ mice, we sought to confirm that ISG$^+$ DCs from both immunocompetent and *Rag2*$^{-/-}$ mice expressed similar transcriptional signatures using bulk RNA-seq (Figure 3J; Table S3). Cells from the scRNA-seq dataset that scored highly for either the *Rag2*$^{-/-}$ ISG$^+$ DC or DC1 signatures were significantly enriched ($p \leq 3.22 \times 10^{-8}$) in their corresponding clusters of our scRNA-seq dataset (Figures 3K, 3L, S3B, and S3C), which validated our flow panel and gating strategy. Cells that scored highly for the WT ISG$^+$ DC signature were also significantly enriched ($p = 7.79 \times 10^{-6}$) in the c2_ISG$^+$ DC scRNA-seq cluster (Figures 3K and 3L). In a pairwise analysis against other clusters, the c2_ISG$^+$ DC cluster consistently scored higher for both the *Rag2*$^{-/-}$ and WT ISG$^+$ DC signatures (Figure S3D) with $p \leq 7.47 \times 10^{-7}$. We further observed significant enrichment of the *Rag2*$^{-/-}$ ISG$^+$ DC signature (adjusted p [p-adj] ≤ 0.05; $\log_2$FC (fold change) cutoff = 1) in the WT ISG$^+$ DC signature by gene set enrichment analysis (GSEA) (Mootha et al., 2003; Subramanian et al., 2005) (Figure 3M). These data

enabled us to conclude that ISG$^+$ DCs isolated from immunocompetent and *Rag2*$^{-/-}$ mice shared similar transcriptional profiles with each other and with the ISG$^+$ DCs originally identified from scRNA-seq.

To phenotypically characterize ISG$^+$ DCs, we assessed expression of myeloid markers. Given the difficulty of distinguishing DC2s from moDCs by flow cytometry (Guilliams et al., 2014; Merad et al., 2013), we refer to them collectively as DC2/moDCs. Consistent with our sequencing analyses, ISG$^+$ DCs were phenotypically distinct from DC1s, migratory DCs, and pDCs, lacking expression of CD24 and CD103, CCR7, and Siglec H, respectively (Figures 3N and S3E). Rather, they more closely resembled DC2/moDCs, expressing high levels of CD11b and Sirpα (Figures 3N and S3E). Given their transcriptional similarity to Inf-cDC2s (Figures S2G and S2H), we assessed the expression of Inf-cDC2 markers and observed that ISG$^+$ DCs also expressed CD64 and MAR-1, as well as the cDC-specific marker CD26 (Figure 3N). This observation suggests that ISG$^+$ DCs might comprise a specific activation state of DC2s. To confirm the ontogeny of ISG$^+$ DCs, we performed a fate-mapping experiment wherein we transferred sorted CD45.1$^+$ granulocyte-macrophage progenitors (GMPs) or precursor (pre-)DCs into MC57-SIY tumors and assessed their fates at day 3 post-transfer (Figures S3F and S3G). Only the transferred pre-DCs but not GMPs gave rise to ISG$^+$ DCs (Figures S3H–S3L). We further affirmed this observation using zDC-DTR BMC mice. Selective depletion of cDCs via DT administration resulted in an 83% reduction of ISG$^+$ DC numbers (Figures S3M and S3N), confirming their ontogeny as cDCs. To probe whether the ISG$^+$ DC state encompassed DC2s, we used the *Irf4*$^{f/f}$*xItgax*^{Cre} mouse model and validated depletion of splenic DC2s (Figures S3O and S3P). We observed a 62% reduction in ISG$^+$ DCs infiltrating MC57-SIY tumors in *Irf4*$^{f/f}$*xItgax*^{Cre} mice compared to littermate controls (Figures 3O and 3P). The remaining ISG$^+$ DCs in *Irf4*$^{f/f}$*xItgax*^{Cre} mice are likely attributable to incomplete Cre recombination efficiency, although IRF4-independent DC2s may also contribute to the ISG$^+$ DC cluster. Thus, these results indicate that most ISG$^+$ DCs are indeed IRF4-driven DC2s.

Importantly, using a recent resource publication on human tumor-infiltrating myeloid cells (Cheng et al., 2021), we observed that cells scoring highly for the ISG$^+$ DC signature were significantly enriched ($p = 3.86 \times 10^{-123}$) in the c5_cDC2_ISG15 cluster (Figure 3Q), indicating that an ISG$^+$ DC-like population can be found in human tumors. Furthermore, the c5_cDC2_ISG15 cluster was significantly enriched for the ISG$^+$ DC signature ($p \leq 1.57 \times 10^{-29}$) in a pairwise comparison against other clusters. In our re-analysis of the Cheng et al. (2021) dataset restricted to tumor-derived cells, we also observed a similar enrichment ($p = 3.04 \times 10^{-106}$) in the c5_cDC2_ISG15 cluster (Figures 3R and S3Q). It is noteworthy that most cells in Cheng et al. (2021) c5_cDC2_ISG15 cluster were derived from a single patient with renal cell carcinoma, which is a relatively immunogenic cancer type (Heidegger et al., 2019). As we also identified ISG$^+$ DCs in the immunogenic MC57-SIY tumor, it is conceivable that the presence of ISG$^+$ DCs may be restricted to highly immunogenic tumors. This notion might explain why they are not detected in most of the previously published human tumor scRNA-seq datasets. Nonetheless, the observation of the ISG$^+$ DC signature in a cluster of human tumor-infiltrating DC2s indicates that they may contribute to anti-tumor immunity against human tumors.

ISG$^+$ DCs acquire and present tumor antigens by MHC class I dressing

To elucidate whether ISG$^+$ DCs were capable of activating CD8$^+$ T cells, we evaluated their stimulatory ability using the *ex vivo* co-culture assay (Figure 4A). ISG$^+$ DCs induced similar levels of 2C T cell expansion as DC1s and to a significantly higher degree than DC2/moDCs (Figure 4B). This observation suggests that in MC57-SIY tumors, the stimulatory DC fraction primarily comprises DC1s and ISG$^+$ DCs. As it is well-established that DC1s excel at cross-presenting cell-associated antigens to prime CD8$^+$ T cells compared to DC2s and other subsets (Broz et al., 2014; Edelson et al., 2010; Hildner et al., 2008; Iyoda et al., 2002), our observations from the co-culture assays prompted us to interrogate the mechanism of antigen presentation used by ISG$^+$ DCs. Two routes of cross-priming of CD8$^+$ T cells have been reported: (1) cross-presentation of exogenously derived antigens (i.e., dead cell debris) and (2) MHC class I dressing, wherein DCs acquire and display intact pMHC class I complexes derived from adjacent cells (Embgenbroich and Burgdorf, 2018). Studies initially described the phenomenon of MHC class I-dressing between virally infected and non-infected DCs *in vivo* (Wakim and Bevan, 2011), but there is increasing evidence for MHC class I dressing as a means of antigen presentation in the tumor context (Das Mohapatra et al., 2020; Nakayama et al., 2021; Squadrito et al., 2018).

We have thus far demonstrated that systemic anti-tumor T cell responses against MC57-SIY tumors are preserved in DC1-deficient *Batf3*$^{-/-}$ mice (Figures 1I and 4C and 4D, #1 and 2). As the only other major stimulatory DC in the tumor (Figure 4B), ISG$^+$ DCs likely drive these responses in *Batf3*$^{-/-}$ mice. Therefore, by using the T cell response in *Batf3*$^{-/-}$ mice as a readout of activation by ISG$^+$ DCs, we could infer their specific mode of antigen presentation. To probe whether the preserved T cell responses in *Batf3*$^{-/-}$ mice were attributable to MHC class I dressing, we generated MC57-SIY tumor cells lacking MHC class I expression by CRISPR-Cas9-mediated deletion of *B2M* encoding the β_2-microglobulin (β2M) subunit. We validated outgrowth of this line in WT mice (Figure S4A). In contrast to MC57-SIY, implantation of MC57-SIY-*B2M*$^{-/-}$ into Batf3$^{-/-}$ mice led to complete loss of systemic anti-tumor T cell responses by IFN-γ ELISpot (Figures 4C and 4D, #3). This observation suggested that ISG$^+$ DCs failed to induce a T cell response when they were precluded from acquiring pMHC class I complexes from the tumor. One possible alternative explanation is the contribution from direct priming by the tumor cells themselves; however, our previous data demonstrating complete ablation of anti-tumor T cell responses in *Itgax-DTR* BMC and zDC-DTR BMC mice effectively excluded this possibility (Figures 2D, 2E, S2A, and S2B). As an additional control to ensure that antigen from MC57-SIY-*B2M*$^{-/-}$ cells could be cross-presented in a WT host, we implanted MC57-SIY-*B2M*$^{-/-}$ cells into WT mice and indeed observed induction of a systemic T cell response (Figures 4C and 4D, #4). Taken together, these data led us to hypothesize that ISG$^+$ DCs were activating CD8$^+$ T cells by MHC class I dressing with tumor-derived pMHC class I complexes.

We used several complementary approaches to validate that ISG$^+$ DCs were indeed capable of MHC class I dressing. We generated *B2M*$^{-/-}$ BMC mice wherein the host immune cells lacked MHC class I molecules (Figures 4E and S4B). Here, cross-presentation is not possible due to the lack of host MHC class I, and therefore CD8$^+$ T cell activation is dependent on MHC class I dressing by DCs. Implanting MC57-SIY cells into *B2M*$^{-/-}$

BMC mice and profiling the tumor-infiltrating DCs, we detected the highest levels of tumor-derived H-2K^b complexes on the surface of *B2M*$^{-/-}$ ISG$^+$ DCs compared to other DC subsets (Figures 4F and 4G). Furthermore, the systemic anti-tumor T cell response in *B2M*$^{-/-}$ BMC mice was comparable to the response in WT BMC mice (Figure 4H), thus providing additional evidence for the contribution of MHC class I-dressed ISG$^+$ DCs to anti-tumor immunity.

To affirm that ISG$^+$ DCs are MHC class I dressing, we established a complementary *in vivo* transfer assay in which we implanted the MC57-SIY tumor line (H-2^b) into MHC class I haplotype mismatched BALB/c mice (H-2^d) (Figure 5A). For these experiments, MC57-SIY cells were engineered to express the ovalbumin-derived model antigen SIINFEKL (SIIN) to allow detection of transferred tumor-derived H-2K^b:SIIN complexes to BALB/c DCs using the antibody 25-D1.16 (Porgador et al., 1997). Specificity of the 25-D1.16 antibody was validated using an isotype control and a SIIN-negative tumor cell line (Figures 5B and 5C). Following implantation of MC57-SIIN-SIY cells into BALB/c mice, we detected the highest levels of tumor-derived H-2K^b:SIIN complexes on the surface of BALB/c ISG$^+$ DCs, indicating that they are indeed most efficient at MHC class I dressing (Figures 5B and 5C). Of note, DC1s were able to acquire some appreciable amount of H-2K^b:SIIN complexes, but this was significantly lower compared to the levels on ISG$^+$ DCs. Implanting MC57 parental cells into BALB/c mice, the highest levels of H-2K^b complexes were again detected on the surface of BALB/c ISG$^+$ DCs compared to other DC subsets (Figures S5A–S5C), showing that MHC class I dressing was independent of a model antigen. To visualize the transfer of tumor-derived pMHC class I complexes *ex vivo*, we sorted ISG$^+$ DCs from BALB/c mice bearing parental MC57 tumors and co-cultured them *ex vivo* with MC57-SIIN-SIY tumor cells (Figure S5D). Using immunofluorescence microscopy, we confirmed the presence of tumor-derived H-2K^b:SIIN complexes on BALB/c ISG$^+$ DCs, indicating they can MHC class I dress *ex vivo* (Figure S5E).

MHC class I-dressed ISG$^+$ DCs can induce protective systemic anti-tumor T cell immunity

We next aimed to determine whether MHC class I dressing could activate CD8$^+$ T cells. DC subsets were sorted from MC57-SIIN-SIY (H-2^b) tumors in BALB/c mice (H-2^d) and co-cultured with OTI TCR transgenic CD8$^+$ T cells (Figure 5D). Due to the mismatched haplotypes in this co-culture system, OTI T cells can only be activated by MHC class I-dressed BALB/c DCs. Consistent with their higher degree of MHC class I dressing with H-2K^b:SIIN complexes (Figures 5B and 5C), BALB/c ISG$^+$ DCs induced the greatest OTI T cell activation (Figures 5E and 5F). In contrast, OTI T cell activation by BALB/c DC1s and DC2/moDCs was weaker (Figures 5E and 5F) in accordance with the lower levels of H-2K^b:SIIN complexes on these DC subsets (Figures 5B and 5C).

To assess whether MHC class I-dressed ISG$^+$ DCs could induce systemic immunity in the absence of DC1s, we performed contralateral flank experiments. MC57-SIY cells were implanted into the flank of *Batf3*$^{-/-}$ mice to initiate the anti-tumor immune response by ISG$^+$ DCs. Six days later, we implanted secondary MC38-SIY cells on the contralateral flank and evaluated their outgrowth (Figure 5G). SIY-specific CD8$^+$ T cells induced by ISG$^+$ DCs were able to control the growth of MC38-SIY tumors, with a 90% decrease in average

tumor burden compared to control at endpoint (Figure 5H). While none of the mice in the control group was tumor-free, 4 out of 15 mice from the MC57-SIY group had completely eradicated their MC38-SIY tumors. The eventual outgrowth of MC38-SIY tumors in all analyzed mice from the MC57-SIY group was due to loss of the shared SIY antigen (Figure S5F). Importantly, implanting MC57-SIY-*B2M*$^{-/-}$ tumor cells (lacking MHC class I for MHC class I dressing) in *Batf3*$^{-/-}$ mice (Figure 5I) completely failed to induce protective immunity, which enabled MC38-SIY tumors on the contralateral flank to grow similar to the control (Figure 5J). Collectively, these observations confirmed that MHC class I-dressed ISG^{+} DCs contribute to anti-tumor CD8^{+} T cell immunity.

IFNAR signaling in the MC57-SIY tumor microenvironment (TME) drives ISG^{+} DC activation

We next aimed to understand how the functional ISG^{+} DC state was induced. Our data demonstrated that while anti-tumor T cell responses in MC57-SIY tumors were driven by both DC1s and ISG^{+} DCs, those against MC38-SIY tumors were solely dependent on DC1s (Figures 1H and 1I). This observation prompted us to interrogate whether ISG^{+} DCs could be found in MC38-SIY tumors. While ISG^{+} DCs could be detected, MC57-SIY tumors showed 5.6-fold higher numbers of ISG^{+} DCs compared to MC38-SIY tumors (Figure 6A). When DCs sorted from MC38-SIY tumors were evaluated in our *ex vivo* co-culture assay (Figure 6B), only DC1s and not ISG^{+} DCs or DC2/moDCs were stimulatory, which is consistent with our data indicating that T cell responses are fully dependent on DC1 (Figure 6C).

The strong IFN response signature characterizing ISG^{+} DCs (Figure 2G) indicates that they are likely sensing IFN-I. IFN-I proteins are secreted by many cell types upon engagement of pattern recognition receptors (PRRs) (Fuertes et al., 2013; Musella et al., 2017; Zitvogel et al., 2015). In the tumor context, activation of STING-dependent cytosolic DNA sensing in innate immune cells is reported to be the predominant PRR that drives IFN-I production (Fuertes et al., 2013; Liu et al., 2018; Woo et al., 2014). To assess the contribution of the host STING pathway to anti-tumor immunity, we implanted MC57-SIY cells into *Sting1*$^{-/-}$ mice but found that that the tumors still regressed with similar kinetics as in WT mice (Figure 6D). This observation suggests that the IFN-I response in MC57-SIY tumors likely does not derive from STING-activated immune cells.

Several studies have demonstrated that tumor cell-derived IFN-I can induce an inflamed tumor microenvironment (Musella et al., 2017; Trujillo et al., 2018; Zitvogel et al., 2015). Accordingly, tumor cells can evolve to suppress cell-intrinsic IFNAR signaling to favor immune evasion (Albacker et al., 2017; Bidwell et al., 2012; Katlinskaya et al., 2016; Katlinski et al., 2017; Linsley et al., 2014). The differences in ISG^{+} DCs from MC57-SIY and MC38-SIY tumors together with our finding that anti-tumor immunity against MC57-SIY was STING-independent prompted us to interrogate whether differential tumor cell-intrinsic IFNAR signaling was a contributing factor. We analyzed the expression of IFN-I and ISG transcripts and observed that MC57-SIY cells expressed higher transcripts of *IFNβ1*, *Irf7*, and *Isg15* compared to MC38-SIY cells at steady state, indicating constitutive IFNAR signaling (Figure 6E). As IFN-I is a secreted cytokine, we next determined whether the amount of IFN-I present in tumor cell-conditioned media was enough to elicit a DC-

intrinsic IFN-I response. To this end, we used WT bone marrow-derived DCs (BM-DCs) (Mayer et al., 2014) and stimulated them overnight with tumorconditioned media. Consistent with their higher expression of IFN-related transcripts, the MC57-SIY conditioned media strongly induced the expression of *IFNβ1*, *Irf7*, and *Isg15* transcripts in BM-DCs, similar to levels induced by the STING agonist DMXAA (Figure 6F). In contrast, the expression in BM-DCs cultured in MC38-SIY conditioned media was more comparable to unstimulated BM-DCs (Figure 6F). To confirm the role of tumor-derived IFN-I, we generated IRF3-deficient MC57-SIY cells using CRISPR-Cas9, which rendered them incapable of producing IFN-I (Figures S6A and S6B) (Sato et al., 2000; Tamura et al., 2008). Importantly, MC57-SIY-*Irf3*$^{-/-}$ conditioned media failed to induce *IFNβ1*, *Irf7*, and *Isg15* transcripts in BM-DCs (Figure 6F), which confirmed that MC57-SIY tumor cells indeed constitutively produced IFN-I.

To determine whether MC57-SIY-derived IFN-I could drive the functional ISG^{+} DC state, we assessed how ablation of IFN-I production via IRF3 deletion would impact anti-tumor immunity. While we still observed rejection in WT mice that was likely mediated by DC1 (Figure S6C), MC57-SIY-*Irf3*$^{-/-}$ tumors grew progressively in *Batf3*$^{-/-}$ mice, which was in contrast to MC57-SIY tumors (Figure 6G). As ISG^{+} DCs are the predominant stimulatory DCs in *Batf3*$^{-/-}$ mice, this observation suggests that tumor-derived IFN-I is critical for driving ISG^{+} DC function. It is possible that IFN-I may be required for the differentiation or recruitment of ISG^{+} DCs. When we analyzed DCs in MC57-SIY and MC57-SIY-*Irf3*$^{-/-}$ tumors, however, no significant differences in numbers or proportion for any DC subset were observed, including ISG^{+} DCs (Figures S6D and S6E). We validated these observations using *Ifnar1*$^{-/-}$ mice. Despite a trend toward reduced frequency of tumor-infiltrating DCs in *Ifnar1*$^{-/-}$ mice compared to WT mice (Figures S6F and S6G), it was not significant, indicating that DC differentiation or recruitment is likely not impacted by IFN-I. Alternatively, IFN-I might induce ISG^{+} DC maturation (Hervas-Stubbs et al., 2011). In MC57-SIY tumors, ISG^{+} DCs are the most mature DCs, expressing the highest levels of CD86, CD80, and CD40 (Figures 6H, S6H, and S6I). To determine whether their maturation state was driven by IFN-I, we generated WT:*Ifnar1*$^{-/-}$ mixed BMC mice (Figure 6I). Indeed, the enhanced maturation of ISG^{+} DCs, and to a lesser degree DC1s and DC2/moDCs, was intrinsically dependent on IFNAR signaling, as indicated by higher expression of CD86 and MHC class II on cells derived from WT BM compared to *Ifnar1*$^{-/-}$ BM (Figures 6J, S6J, and S6K).

As costimulatory signaling is critical for successful T cell activation (Chen and Flies, 2013; Lenschow et al., 1996), we next assessed how impaired maturation of ISG^{+} DCs from MC57-SIY-*Irf3*$^{-/-}$ tumors impacted anti-tumor T cell responses. While anti-tumor T cell responses were still induced in WT mice, likely by DC1s, ISG^{+} DCs from MC57-SIY-*Irf3*$^{-/-}$ tumors failed to mount anti-tumor T cell responses in *Batf3*$^{-/-}$ mice (Figures 6K and 6L). Taken together, these data indicate that in MC57-SIY tumors ISG^{+} DCs are activated by tumor-derived IFN-I to drive anti-tumor CD8^{+} T cell responses.

Exogenous addition of IFN-β to progressor tumors restores anti-tumor T cell responses in *Batf3*$^{-/-}$ mice via activation of MHC class I-dressed ISG^{+} DCs

Our data suggest that tumor cell-derived IFN-I is a driving factor for the induction of the functional ISG^{+} DC state. To determine whether this observation was generalizable, we screened a panel of murine and human tumor lines for constitutive IFNAR signaling at baseline. While the vast majority of tumor lines did not exhibit spontaneous IFNAR signaling, a handful did express IFN-I and ISG transcripts at steady state, similar to MC57-SIY cells (Figures 7A, 7B, S7A, and S7B). We sorted DC subsets from one such IFN-I/ISG-expressing tumor, the fibrosarcoma 1969-SIY, and evaluated them in our *ex vivo* co-culture assay (Figure S7C). Similar to our observations from MC57-SIY tumors, both DC1s and ISG^{+} DCs from 1969-SIY tumors induced robust 2C T cell proliferation (Figure S7D). Systemic anti-tumor T cell responses against 1969-SIY were also preserved in the absence of DC1 (Figure S7E). Thus, these data indicate that ISG^{+} DCs are contributors to anti-tumor T cell responses in tumors that constitutively produce IFN-I.

As evident from our IFN-I and ISG screens, most tumor cell lines do not exhibit constitutive IFNAR signaling at steady state (Figures 7A, 7B, S7A, and 7SB) and are thus unlikely to harbor stimulatory ISG^{+} DCs. To determine whether we could induce functional ISG^{+} DCs, we co-injected progressor MC38-SIY cells with or without recombinant murine IFN-β into the flanks of *Batf3*$^{-/-}$ mice and assessed for the rescue of systemic anti-tumor T cell responses as a readout for ISG^{+} DC activation (Figure 7C, #1–3). Whereas implantation of MC38-SIY tumor cells alone failed to mount a T cell response in the absence of DC1, co-injection with IFN-β resulted in rescue of the systemic anti-tumor T cell response to 84% of what is observed in WT mice (Figures 7C and 7D, #1–3). MC38-SIY tumors co-injected with IFN-β in *Batf3*$^{-/-}$ mice were more infiltrated with functional SIY-specific CD8^{+} T cells (Figure S7F) and ISG^{+} DCs that exhibited higher expression of CD86 and CD80 (Figures S7G–S7I). We further assayed whether the restored T cell response was dependent on MHC class I dressing as a functional readout for ISG^{+} DCs. To this end, we co-injected MHC class I-deficient MC38-SIY-*B2M*$^{-/-}$ tumor cells with IFN-β and implanted them into *Batf3*$^{-/-}$ mice (Figure 7C, #4). Strikingly, we observed that when ISG^{+} DCs were precluded from acquiring tumor-derived pMHC class I (via *B2M*$^{-/-}$ tumor), there was no rescue of T cell responses in *Batf3*$^{-/-}$ mice despite the presence of IFN-β (Figures 7C, 7D, #4 and S7F). These data indicate that exogenously added IFN-β can activate ISG^{+} DCs, which rely on MHC class I dressing to drive CD8^{+} T cell responses. Importantly, IFN-β-mediated activation of ISG^{+} DCs in *Batf3*$^{-/-}$ mice could also rescue functional anti-tumor immunity against parental MC38 tumors (Figures S7J–S7M). We further extended these observations to the poorly immunogenic B16-SIY melanoma model, another progressor tumor that did not exhibit constitutive IFN-I production at baseline (Figures 7A and S7A). B16-SIY tumors also exhibited rescued T cell responses in *Batf3*$^{-/-}$ mice when co-injected with exogenous IFN-β (Figures 7E and 7F). Collectively, our data demonstrate that it is possible to induce stimulatory DC states that are distinct from DC1 to enhance anti-tumor CD8^{+} T cell immunity in poorly immunogenic tumors.

DISCUSSION

We identified a novel IFN-I-induced activation state of CD11b$^+$ cDCs, which we called ISG$^+$ DCs, that was capable of driving anti-tumor CD8$^+$ T cell immunity by MHC class I dressing with tumor-derived pMHC class I complexes. The contribution of ISG$^+$ DCs to anti-tumor immunity was best discerned using *Batf3*$^{-/-}$ mice. Whereas the absence of DC1 completely ablated anti-tumor CD8$^+$ T cell responses against MC38-SIY tumors, those against MC57-SIY tumors were still induced and capable of driving tumor rejection in *Batf3*$^{-/-}$ mice. We provide evidence that ISG$^+$ DCs were activated by IFNAR signaling in the TME of MC57-SIY tumors. Thus, we speculate that they are most relevant to the immune response in disease settings that trigger a strong IFN-I response, such as in viral infections. Importantly, ISG$^+$ DCs could be induced by addition of exogenous IFN-β to drive anti-tumor CD8$^+$ T cell responses in poorly immunogenic tumors lacking DC1.

Numerous studies have delved into elucidating tumor-intrinsic signaling pathways that suppress anti-tumor immune responses (Nguyen and Spranger, 2020; Spranger and Gajewski, 2018; Yang et al., 2019). We demonstrate in the present study that it is also critical to dissect tumor-intrinsic pathways that are immunostimulatory, as they may yield insights toward modulating the TME to promote productive anti-tumor immune responses. The study of spontaneously regressing tumors proves particularly useful in this context. The stark contrast in the anti-tumor immune response between MC38-SIY and MC57-SIY tumors in *Batf3*$^{-/-}$ mice was mediated by differential tumor cell-intrinsic IFNAR signaling at baseline. MC57-SIY tumor cells exhibited constitutive IFN-I production, whereas MC38-SIY tumor cells did not. The increased presence of IFN-I in the MC57-SIY TME was sufficient to drive the maturation and activation of stimulatory ISG$^+$ DCs. Our screen of murine and human tumor lines revealed that constitutive IFNAR signaling in tumor cells at steady-state is a rather rare phenotype. Accordingly, this may be why the ISG$^+$ DC state has not been widely described in the tumor context.

While we have yet to determine the upstream pathways triggering IFNAR signaling in regressor MC57-SIY tumors, several reports indicate that tumor-intrinsic IFN-I can be induced by the aberrant accumulation of intracellular double-stranded RNA (dsRNA) or cytosolic DNA in tumor cells (Ishizuka et al., 2019; Liu et al., 2019; Schadt et al., 2019; Takahashi et al., 2021). In line with the immunostimulatory effects of IFN-I, these tumors generated more inflamed microenvironments and were more sensitive to immunotherapy (Ishizuka et al., 2019; Liu et al., 2019; Schadt et al., 2019; Takahashi et al., 2021). Although IFN-I has been described to modulate multiple facets of the immune response, it is conceivable that ISG$^+$ DCs activated by IFNAR signaling may contribute to anti-tumor CD8$^+$ T cell responses in these settings. This observation is consistent with the recent report describing the induction of Inf-cDC2s in the context of an IFN-I response triggered by viral infection (Bosteels et al., 2020). While direct comparative studies are needed to determine their degree of relatedness, ISG$^+$ DCs expressed the Inf-cDC2 markers CD26, CD64, and MAR-1. The expression of CD64 and MAR-1 receptors on Inf-cDC2s was reported to be critical for their uptake of viral antigens in the form of immune complexes. While it is possible that CD64 and MAR-1 may also contribute to antigen uptake by ISG$^+$ DCs via Fc receptor-mediated endocytosis, we demonstrate through several complementary experiments

that the major mode of antigen presentation by ISG$^+$ DCs occurs via MHC class I dressing. We offer a couple of lines of reasoning to suggest why ISG$^+$ DCs are particularly adept at MHC class I dressing. First, the phenomenon of CD8$^+$ T cell activation by MHC class I dressing depends on the acquisition of pMHC class I complexes from tumor cells. Thus, the number of pMHC class I complexes expressed on tumor cells is inherently an important factor for whether MHC class I dressing occurs. As IFN-I is a positive regulator of MHC class I expression (Raval et al., 1998), it is conceivable that MC57-SIY cells express higher levels of MHC class I, thereby increasing the probability of MHC class I dressing. Second, MHC class I dressing by DCs has been reported by Wakim and Bevan (2011) during viral infection, which is associated with strong IFN-I induction. The downstream effects of IFNAR signaling in ISG$^+$ DCs might explain their enhanced ability to MHC class I dress. We identified and used AXL solely as a phenotypic marker for ISG$^+$ DCs. However, given that AXL is IFN-inducible and has been reported to be an endocytic receptor (Schmid et al., 2016; Subramanian et al., 2014), it is plausible that AXL might be involved in MHC class I dressing.

It is increasingly important to delineate the individual contributions of distinct DC states to the anti-tumor immune response, as they may be non-redundant. Our work is another example that the functional dichotomy between DC1s and DC2s is not black and white and changes under inflammatory conditions, wherein DC2s and other CD11b$^+$ cDCs can acquire the ability to activate CD8$^+$ T cells. The differing modalities of antigen presentation used by DC1s and ISG$^+$ DCs, cross-presentation and MHC class I dressing, respectively, can have major implications for the resultant anti-tumor T cell response. The density of pMHC class I complexes on DCs, for instance, has been described to impact memory and effector T cell responses (Bullock et al., 2003; Sykulev et al., 2012). It is conceivable that MHC class I dressing might yield a lower density of pMHC class I complexes on the surface of DCs compared to direct or cross-presentation, which would therefore influence T cell priming. ISG$^+$ DCs also express higher levels of costimulatory molecules compared to DC1s, which can diversify T cell activation phenotypes. Additionally, the high expression of *Cxcl10* (an IFN-induced gene) by ISG$^+$ DCs identified through scRNA-seq suggests that they may contribute to T cell recruitment, which is a function that has recently been ascribed to tumor-resident DC1 (Spranger et al., 2017). Accordingly, it is of great interest to investigate the range of T cell responses induced by DC1s or ISG$^+$ DCs and their impact on anti-tumor immunity.

The contribution of ISG$^+$ DCs in the context of cancer therapy warrants further investigation. There is substantial evidence that the success of radiation therapy, chemotherapy, and immunotherapy is dependent on intact IFNAR signaling (Burnette et al., 2011; Sistigu et al., 2014; Zaretsky et al., 2016). As ISG$^+$ DCs are activated by IFN-I, they are likely relevant to the anti-tumor immune response induced by these therapies. Importantly, our data suggest that IFN-I does not have to derive from tumor cells per se. Rather, the total intratumoral IFN-I concentration appears to be the critical factor. This presents an opportunity for therapeutic intervention using tumor-localized IFN-β. It will be interesting to determine whether PRR agonists that drive strong IFN-I responses, such as RIG-I and STING agonists that are currently in clinical development (Iurescia et al., 2020; Le Naour et al., 2020), can also activate ISG$^+$ DCs and enhance anti-tumor T cell

responses. Our work suggests that these IFN-I-related therapies might be most effective in DC1-excluded tumors (Barry et al., 2018; Böttcher et al., 2018) or poorly immunogenic tumors with defective tumor cell-intrinsic IFNAR signaling (Kalbasi and Ribas, 2020; Zaretsky et al., 2016; Zitvogel et al., 2015). Taken together, our work broadens the current knowledge of functional DC states distinct from DC1s that are capable of driving anti-tumor $CD8^+$ T cell responses.

Limitations of study

While our comparative model of a regressor and a progressor tumor facilitated the study of stimulatory DC states, it also has limitations. To broaden our findings, we screened additional murine tumor lines and found that our observations could be extended beyond our model system. Moving forward, it will be critical to assess for ISG^+ DCs in additional murine tumor models and, more importantly, to establish the relevance of ISG^+ DCs in human tumors. Nonetheless, our study demonstrates that IFN-β can be used to induce ISG^+ DCs in poorly immunogenic murine tumors, and it will be interesting to determine whether this therapeutic implication holds true in the human setting.

STAR★METHODS

RESOURCE AVAILABILITY

Lead contact—Further information and requests for resources and reagents should be directed to and will be fulfilled by the lead contact, Stefani Spranger (spranger@mit.edu).

Materials availability—This study did not generate new unique reagents.

Data and code availability—All data is available in the main text or the supplementary materials. The RNA-seq data has been deposited to the GEO database (GSE181939). Any additional information required to reanalyze the data reported in this paper is available from the lead contact upon request.

EXPERIMENTAL MODEL AND SUBJECT DETAILS

Mice—C57BL/6, BALB/c, and *Rag2*$^{-/-}$ mice were purchased from Taconic Biosciences. *Batf3*$^{-/-}$, *B2M*$^{-/-}$, *Itgax*^{Cre}, *Itgax-DTR*, *Clec9a*$^{-/-}$, *Ifnar1*$^{-/-}$, and *Irf4*$^{f/f}$ mice were purchased from Jackson Laboratories and bred in-house. $Irf4^{f/f}$x$CD11c^{Cre}$ mice were obtained by breeding *Irf4*$^{f/f}$ mice and *Itgax*^{Cre} mice to specifically ablate IRF4 in the $CD11c^+$ compartment. T cell receptor transgenic (TCR-tg) 2C *Rag2*$^{-/-}$ and OTI *Rag2*$^{-/-}$ mice were bred and maintained in-house. *Zbtb46-DTR* (zDC-DTR) mice were a gift from the Cyster Lab at UCSF and the Mempel Lab at Harvard/MGH. All mice were housed and bred under specific pathogen free (SPF) conditions at the Koch Institute animal facility. Ifnar1$^{-/-}$ mice were initially housed and bred at the Koch Biology Building animal facility. Following rederivation, Ifnar1$^{-/-}$ mice were bred and maintained at the Koch Institute animal facility. For experiments with Ifnar1$^{-/-}$ mice, only female mice 6–8 weeks old were used. For all other strains, mice were gender-matched and age-matched to be 6–12 weeks old at the time of experimentation. All experimental animal procedures were approved by the Committee on Animal Care (CAC/IA-CUC) at MIT.

Tumor cell lines—Parental and SIY-GFP expressing MC38 colon carcinoma, MC57 fibrosarcoma, 1969 fibrosarcoma, and B16 melanoma tumor cell lines were a gift from the Gajewski laboratory at The University of Chicago. Tumor cell lines were cultured at 37°C and 5% CO_2 in DMEM (GIBCO) supplemented with 10% FBS (Atlanta Biologicals), 1% penicillin/streptomycin (GIBCO), and 1X HEPES (GIBCO). All cell lines were regularly subjected to mycoplasma testing.

METHOD DETAILS

Generation of cerulean-SIIN-SIY expression vector—The pLV-EF1α-IRES-puro vector (Addgene #85132) was digested with BamHI and EcoRI restriction enzymes (NEB) to linearize the vector. The cerulean-SIIN-SIY insert was generated using the Cerulean-N1 vector (Addgene #54742) linked to a codon-optimized sequence of the SIINFEKL (SIIN) and SIYRYYGL (SIY) peptides. The insert was then cloned into the linearized pLV-EF1α-IRES-puro vector (final construct referred to as 'pLV-EF1α-cerulean-SIIN-SIY-IRES-puro') using the In-Fusion cloning kit (Takara Bio), amplified, and sequenced for accuracy.

Generation of CRISPR knockout constructs—The px459-Cas9-puro vector (Addgene #62988) was digested with the *BbsI* restriction enzyme (NEB) to linearize the vector. CRISPR guides targeting exon 2 of murine β−2 microglobulin (β2M) and exons 1–3 of IRF3 were designed using Benchling (Table S5). Forward and reverse oligos (Integrated DNA Technologies) for each guide were annealed together with a standard annealing protocol, cloned into the px459-Cas9-puro vector by T4 ligation (NEB), amplified, and sequenced for accuracy.

Generation of modified tumor cell lines—Parental and SIY-GFP expressing MC38 colon carcinoma, MC57 fibrosarcoma, 1969 fibrosarcoma, and B16 melanoma tumor cell lines were a gift from the Gajewski laboratory at The University of Chicago. The MC57 tumor line stably expressing cerulean-SIIN-SIY was generated by lentiviral transduction of the parental tumor line with the pLV-EF1α-cerulean-SIIN-SIY-IRES-puro construct and puromycin (GIBCO) selected. Expression was confirmed using flow cytometry for cerulean-expressing cells. CRISPR-Cas9-mediated knockout tumor cell lines for *B2M* and *Irf3* were generated by transient transfection with the pooled guide constructs and selected with puromycin for 48 hr. Cells surviving puromycin treatment were expanded, and the ablation of the target gene was confirmed by sequencing, qPCR, and/or western blot.

Tumor outgrowth studies—Tumor cells were harvested by trypsinization (GIBCO) and washed 3 times with 1X PBS (GIBCO). Cells were resuspended in PBS, and 2×10^6 tumor cells were injected subcutaneously into the flanks of mice. Subcutaneous tumor area measurements (calculated as *length* x *width*) were collected 2–3 times a week using digital calipers until the endpoint of the study.

Generation of recombinant IFNβ—Murine *IFNβ1* was cloned with C-terminal His-tags into the gWiz expression vector (Gelantis) using the In-Fusion HD cloning kit (Takara Bio). HEK293 cells were transfected with endotoxin free plasmid DNA (Macherey-Nagel) using OptiPRO serum-free media (GIBCO) and polyethylenimine 25K (Polysciences). Six

days later, proteins were purified from filtered supernatant using TALON metal affinity resin (Takara Bio), eluted with PBS 200 mM imidazole, buffer exchanged into PBS, and sterile-filtered. IFNβ had the correct molecular weight as determined by SDS-PAGE, and < 0.001 endotoxin units per μg as measured by a LAL chromogenic kit (Pierce). IFNβ activity was confirmed using RAW-Lucia ISG Cells (InvivoGen).

***In vivo* IFNβ co-injection—**For *in vivo* experiments involving IFNβ co-injection, 2×10^6 tumor cells were resuspended with 50 μg IFNβ (generated as described above by the Wittrup Lab) in PBS and injected subcutaneously into the flanks of mice.

***In vivo* depletion of cytolytic cells—**To deplete Natural Killer (NK) cells, 50 μg of anti-NK1.1 (Bio X Cell) or an isotype control antibody (Bio X Cell) was injected intraperitoneally 2 days prior to tumor implantation and subsequently every 3–4 days thereafter for the duration of the study. To deplete T cells, 200 μg of anti-CD8 (Bio X Cell), anti-CD4 (Bio X Cell), combined anti-CD8/anti-CD4, or an equal volume of PBS was injected intraperitoneally 2 days prior to tumor implantation, and 100 μg was subsequently injected every 3–4 days thereafter for the duration of the study.

IFNγ ELISpot—ELISpot plates (EMD Millipore) were coated overnight at 4°C with anti-IFNγ (BD Biosciences). Plates were washed and blocked with DMEM supplemented with 10% FBS, 1% penicillin/streptomycin, and 1X HEPES for 2 hr at room temperature (RT). Spleens were harvested from mice at day 5 or day 7 post-tumor inoculation and mashed through a 70 μm filter with a 1 mL syringe plunger to generate a single cell suspension. Red blood cells were lysed with 500 mL of ACK Lysing Buffer (GIBCO) on ice for 2 min and splenocytes were washed 3 times with chilled PBS. For IFNγ-ELISpot assays using SIY peptide restimulation, 1×10^6 splenocytes were assayed per well in the presence or absence of 160 nM SIY peptide. For IFNγ-ELISpot assays using irradiated parental tumor cell debris for restimulation (Figures S7I–S7K), 3×10^6 splenocytes were assayed per well in the presence or absence of 1×10^5 parental tumor cells that were irradiated a day prior with 4000 rad. As a positive control, splenocytes were incubated with a mixture of 100 ng/mL PMA (Sigma-Aldrich) and 1 μg/mL ionomycin (Sigma-Aldrich). Following an overnight incubation at 37°C and 5% CO_2, plates were developed using the BD mouse IFNγ-ELISpot kit, following manufacturer's protocol.

Generation of bone marrow (BM) chimeric mice—Host mice were irradiated with 500 rad, allowed to recover for 3 hr, and subsequently irradiated again with 550 rad. The next day, BM was harvested from the femur and tibia of donor mice, washed and resuspended in PBS, and 1×10^7 cells were injected retro-orbitally into the irradiated host mice. For mixed BM chimeras, 1×10^7 total cells of a 50:50 mixture of BM from donor mice was transferred. A period of 8 weeks was allowed for engraftment prior to the start of experiments.

DT-mediated depletion—For depletion of DC in *Itgax-DTR*, *Itgax-DTR:Ifnar1*$^{-/-}$, and zDC-DTR BM chimeras, 500 ng diphtheria toxin (DT) (Sigma-Aldrich) (or an equivalent volume of PBS for control mice) was injected intraperitoneally 2 days prior to tumor implantation and subsequently injected every other day thereafter for 7 days.

Tumor dissociation—Tumors were dissected from mice, weighed, and collected in 500 μL RPMI (GIBCO) containing 250 μg/mL Liberase (Sigma-Aldrich) and 50 μg/mL DNase (Sigma-Aldrich). Tumors were minced with dissection scissors and incubated for 20 min at 37°C for enzymatic digestion. Following the digestion, tumor pieces were mashed through a 70 μm filter with a 1 mL syringe plunger to generate a single cell suspension. The dissociated cells were washed 3 times with chilled PBS containing 1% FBS and 2 mM EDTA (GIBCO).

Flow cytometry and cell sorting—Prior to staining, cells were washed with FACS staining buffer (chilled PBS containing 1% FBS and 2 mM EDTA). Cells were stained for 15 min on ice with eBioscience Fixable Viability Dye eFluor 780 to distinguish live and dead cells and with anti-CD16/CD32 (clone 93, BioLegend) to prevent non-specific antibody binding. Cells were then washed once and cell surface proteins were stained for 30 min on ice with fluorophore-conjugated antibodies at the specified dilutions (Table S5). For stains that used biotinylated primary antibodies, cells were washed twice and subsequently stained with a streptavidin-conjugated fluorophore for 30 min on ice. Following the surface staining, cells were washed twice and analyzed directly or fixed with IC Fixation Buffer (eBioscience) for 20 min at RT for analysis the next day. To obtain absolute counts of cells, Precision Count Beads (BioLegend) were added to samples following manufacturer's instructions. Flow cytometry sample acquisition was performed on a BD LSRFortessa cytometer, and the collected data was analyzed using FlowJo v10.5.3 software (TreeStar). For cell sorting, the surface staining was performed as described above under sterile conditions, and cells were acquired and sorted into RPMI containing 10% FBS, 1% penicillin/streptomycin, and 1X HEPES using a BD FACSAria III sorter.

SIY-pentamer staining—To identify SIY-reactive $CD8^+$ T cells, samples were stained with a 1:100 dilution of a PE-conjugated SIY pentamer (ProImmune) for 30 min on ice. The pentamer was added during the surface staining step in the flow cytometry methods described above.

Progenitor transfer fate-mapping experiment—To expand pre-DC, $CD45.1^+$ C57BL/6 mice were injected every other day with 10 μg recombinant human Flt3L-Ig (Bio X Cell). BM was then harvested from the femur and tibia of mice by flushing the bones with RPMI using a 1 mL syringe. Cells were passed through a 70 μm filter, washed twice with PBS, and subjected to flow cytometry staining and sorting as described above. GMP were sorted as live $CD45.1^+$, $lineage^-$ (CD19, CD3e, NK1.1, MHC-II, CD11c), $Sca\text{-}1^-$, $c\text{-}Kit^+$, $Flt3^-$, $CD16/32^+$, $CD11b^+$, $Ly6C^+$. Pre-DC were sorted as live $CD45.1^+$, $lineage^-$ (CD19, CD3e, NK1.1, MHC-II), $Sca\text{-}1^-$, $c\text{-}Kit^-$, $CD16/32^-$, $Flt3^+$, $CD11c^+$. Equal numbers of GMP or pre-DC were injected *i.t.* into MC57-SIY tumor-bearing $CD45.2^+$ $Rag2^{-/-}$ host mice at day 11 post-tumor implantation. At 3 days post-transfer, MC57-SIY tumors were harvested and the fates of the transferred cells were analyzed by flow cytometry.

Staining for *in vivo* MHC class I dressing assay—Related to Figures 4E–4G, 5A–5C, and S5A–S5C. Surface flow staining for $H\text{-}2K^b$ or $H\text{-}2K^b$:SIIN on the DC infiltrate of dissociated tumors was performed as follows: Cells were stained for 15 min on ice

with eBioscience Fixable Viability Dye eFluor 780 and blocked with anti-CD16/CD32 (clone 93, BioLegend) and BV786 anti-CD64 (clone X54–5/7.1, BD Biosciences) to prevent non-specific antibody binding. Cells were then washed once and cell surface proteins were stained as described above. For detection of H-2K^b, PE-Cy7 anti-H-2K^b (clone AF6–88.5, BioLegend) was used at a 1:200 dilution. For detection of H-2K^b:SIIN, biotinylated anti-H-2K^b:SIIN (clone 25-D1.16, eBioscience) (Porgador et al., 1997) or a biotinylated isotype control (clone 2016875, eBioscience) was used at a 1:200 dilution, followed by a streptavidin-BV711 secondary at a 1:400 dilution. Specificity for H-2K^b or H-2K^b:SIIN staining was validated using a Fluorescence Minus One (FMO) control, an antigen-irrelevant tumor line, and/or an isotype control.

MHC class I dressing visualization by immunofluorescence microscopy— MC57-SIY (H-2^b) tumor cells were implanted into the flanks of WT BALB/c mice (H-2^d). On day 5 post-tumor inoculation, BALB/c ISG$^+$ DC were sorted from dissociated tumors, as described previously. Coverslips in 6-well non-TC-treated plates were coated with 500 μL Poly-L-Lysine (GIBCO) for 10 min at RT, washed 3 times with sterile water, and air-dried. Sorted BALB/c ISG$^+$ DC and MC57-SIIN-SIY tumor cells at a 1:1 ratio, or separately as controls, were plated on the coverslips and cultured for 24 hr at 37°C and 5% CO_2 in RPMI supplemented with 10% FBS, 1% penicillin/streptomycin, 1X HEPES, 1X MEM Non-Essential Amino Acids, and 1X β-mercaptoethanol. After 24 hr, cells were fixed with 4% paraformaldehyde for 20 min at RT and gently permeabilized with 0.1% Triton X-100 (Sigma-Aldrich) for 10 min at RT. Coverslips were then blocked with 2.5% bovine serum albumin (Research Products International) and anti-CD16/CD32 (clone 93, BioLegend) for 20 min at RT. Primary antibodies at a 1:200 or a 1:400 dilution (Table S4) were added to the coverslips and incubated for 1 hr at RT. Coverslips were then washed 3 times with Dulbecco's PBS with calcium and magnesium (GIBCO) for 5 min each. Secondary antibodies (Table S5) were added at 1:400 dilution and incubated for 20 min at RT. Following washes, coverslips were mounted onto glass slides using ProLong Gold Antifade with DAPI (Invitrogen). Slides were dried overnight, sealed with clear nail polish, and imaged using a Leica TCS SP8 confocal laser scanning microscope.

***Ex vivo* APC/DC-T cell co-culture assay—**To obtain antigen-presenting cell compartments or specific DC subsets, cells were FACS-sorted from tumors as described above. To obtain CD8$^+$ T cells, TCR transgenic CD8$^+$ T cells were isolated from spleen and lymph nodes of naive 2C or OTI TCR transgenic *Rag2*$^{-/-}$ mice using a CD8$^+$ T cell isolation kit (Miltenyi Biotec), following manufacturer's instructions. Isolated CD8$^+$ T cells were washed twice with PBS and stained with 2.5 μM CFSE (eBioscience) in PBS for 8 min at 37°C or 5 μM CellTrace Violet (Thermo Fisher Scientific) in PBS for 20 min at 37°C. The dye was then quenched with FBS, and the cells were washed 3 times with RPMI containing 10% FBS. For the co-culture, 5×10^5 dye-labeled TCR transgenic CD8$^+$ T cells and 1×10^5 sorted antigen-presenting cells or DCs (5:1 T cell-DC ratio) were mixed and added to each well of a V-bottom tissue culture-treated 96-well plate in RPMI supplemented with 10% FBS, 1% penicillin/streptomycin, 1X HEPES, 1X MEM Non-Essential Amino Acids (GIBCO), and 1X β-mercaptoethanol (GIBCO). The cells were cultured at 37°C and 5% CO_2 for 72 hr at which point T cell proliferation was measured by dye dilution via flow

cytometry as a proxy for T cell activation. To determine the replication indices per condition, gates for each individual proliferation peak were manually drawn in FlowJo to obtain cell counts per round of division. The replication indices per condition were then calculated as: total number of divided cells / total number of cells that underwent division. Expression of T cell activation markers and cytokines was also assessed by flow staining as described.

scRNA-seq and analysis—Live intratumoral CD45$^+$ cells from *Rag2*$^{-/-}$ mice bearing MC57-SIY tumors at day 7 post-tumor implantation were FACS-sorted as described above. Sorted cells were washed twice and resuspended at a final concentration of 1×10^3 cells/μL in chilled PBS containing 0.04% BSA (Thermo Fisher Scientific). The cellular suspension was submitted to the Whitehead Institute Genome Technology Core for cDNA library preparation. Briefly, single cells were encapsulated into droplets using the 10X Genomics Chromium Controller, and the cDNA library was prepared using the Chromium Single Cell 3′ Reagent Kits v2 (10X Genomics) following manufacturer's instructions. The resultant cDNA library was then sequenced by the MIT BioMicro Center using an Illumina HiSeq2000. Demultiplexing, mapping to the mm10 genome, and barcode and UMI counting were performed with 10X Genomics Cell Ranger v3.0.1, and the resultant count matrix was loaded into Seurat v3.2.2 (Butler et al., 2018) for further processing. Cells expressing less than 200 genes or more than 4500 genes, as well as cells expressing more than 25% mitochondrial transcripts were excluded, which left 6262 cells for downstream analysis. The data was normalized using the Seurat LogNormalize function with the default scale factor of 10^4. The data was subsequently scaled using the Seurat ScaleData function and latent variables (number of UMIs and percentage of mitochondrial transcripts) were regressed out. The Seurat FindVariableGenes function was used to identify 2000 variable genes for principal component analysis (PCA). The Seurat FindClusters function, which implements the shared nearest neighbor (SNN) clustering algorithm, identified 15 clusters using the top 17 PCA components and a resolution of 0.8. The Seurat FindAllMarkers function was used to identify the differentially expressed genes (DEG) for each cluster compared to all other clusters with default parameters that required genes to be expressed in more than 25% of cells with a minimum 0.5-fold difference (Table S1). To identify clusters, we manually compared the DEG lists of our clusters to reports in the literature.

scRNA-seq DC population analysis and ISG$^+$ DC surface marker identification —To examine DC at higher resolution, we computationally isolated cell clusters that expressed a canonical DC signature (*H2-Ab1* and *Itgax* and *Flt3*) using the Seurat SubsetData function (clusters 4, 12, 13, 15). The initial analysis using Seurat identified a contaminating macrophage cluster expressing *Adgre1, Mafb,* and *C5ar1* (cluster 3), which was subsequently excluded during another round of filtering. The remaining cells were then passed through the Seurat analysis pipeline as described above which led to the identification of seven DC clusters (711 cells) using 2000 variable genes, the top 12 PCA components, and a resolution of 0.8 (Table S2). To identify clusters, we manually cross-referenced the DEG lists of the DC clusters to the DC signatures recently reported in the literature (Guilliams et al., 2016; Merad et al., 2013; Mildner and Jung, 2014; Murphy et al., 2016; Zilionis et al., 2019). To validate our manual cluster assignments, we scored each cell in our dataset using the AddModuleScore function (Tirosh et al., 2016) for expression

of DC subset gene signatures that were either published (Zilionis et al., 2019) or generated from an analysis of a publicly available dataset (GSM4505993) (Bosteels et al., 2020) (Table S3). To identify surface markers for cluster 2 (ISG^+ DC) for downstream functional studies, we filtered the DEG list for cluster 2 and required that marker genes must (1) have a minimum avg_logFC threshold of 0.5; (2) have an adjusted *p-value* < 0.05; (3) be unique to cluster 2; (4) have an enrichment score < 0.5, defined as the ratio of percent expression in all other clusters (pct.2) versus percent expression in cluster 2 (pct.1), (5) be surface-expressed; and (6) have a commercially available antibody (Table S4).

Generation of Bosteels et al. DC signatures—To generate the Bosteels DC signatures for non-mig. cDC2 and Inf-cDC2, we downloaded the "CD45.1 WT derived cells from WT:WT chimeric mice" dataset from the Gene Expression. Omnibus database under accession number GSM4505993 (Bosteels et al., 2020). The dataset was analyzed with the Seurat package as described above, using the top 15 PCA components and a resolution of 0.4 to cluster the cells. Cluster identities were assigned by cross-referencing DEG from each cluster with the published marker genes (Bosteels et al., 2020). The top 20 DEG for non-mig. cDC2 and Inf-cDC2 (Table S3) were used to generate the signatures used in the AddModuleScore analysis.

Bulk RNA-seq and analysis—ISG^+ DC and $CD103^+$ DC1 were FACS-sorted from MC57-SIY tumors in WT and *Rag2*$^{-/-}$ mice at day 7 post-implantation as described above using the gating strategies shown in Figures 3B and S3B. Cells were sorted directly into TRIzol (Invitrogen), and RNA was isolated using a TRIzol-chloroform extraction. The RNA-containing aqueous layer was collected, purified using the RNeasy MinElute Cleanup Kit (QIAGEN) following manufacturer's instructions, and submitted to the MIT BioMicro Center for library preparation (Clontech ZapR) and sequencing (Illumina NextSeq500). Paired-ended 38-mer RNA-seq reads were pre-processed to trim five low-quality read positions from the second read (R2) of each pair, using the FASTX-Toolkit (Hannon Lab, CSHL). Reads were then mapped to the USCC mm9 mouse genome build (genome.ucsc.edu) using Bowtie v1.2.3 (Langmead et al., 2009) and gene counts were quantified using RSEM v1.3.1 (Li and Dewey, 2011). Estimated expression counts generated by RSEM were used to detect differentially expressed (DE) genes (p-adj ≤ 0.05) between pairwise conditions (*Rag2*$^{-/-}$ ISG^+ DC versus *Rag2*$^{-/-}$ DC1; WT ISG^+ DC versus *Rag2*$^{-/-}$ DC1) using DESeq2 v1.26.0 (Love et al., 2014) with a 2X fold-change cutoff per comparison (Table S3). Pairwise signature enrichment was analyzed using the pre-ranked mode in GSEA v4.1.0 (Subramanian et al., 2005). The AddModuleScore function (Tirosh et al., 2016) in Seurat (Butler et al., 2018) was used to score cells from the scRNA-seq dataset for enrichment of the bulk RNA-seq-derived DC signatures. Each cell in the scRNA-seq UMAP plot was then colored by its enrichment score for the bulk RNA-seq signatures.

Re-analysis of dataset from Cheng et al. (Cell 2021)—A normalized expression matrix of scRNA-seq counts for the cDC2 dataset was retrieved from GEO (accession GSE154763) along with associated metadata per cell and processed with Seurat v3.2 (Stuart et al., 2019). A Seurat object was created such that the counts slot and data slot were populated with the library-size corrected counts and log-transformed normalized counts,

respectively. The dataset was filtered (based on metadata annotation) to retain only cells from tumor samples. Only twenty patient samples with over 30 cells were selected and used for downstream analyses. Seurat's reference-based integration approach (Stuart et al., 2019) was used to hierarchically integrate samples, first per patient and then across patients. Dimensionality reduction with PCA and UMAP embeddings (with the top 35 principal components) were generated using the integrated dataset. The Seurat default "RNA" assay with log-transformed normalized counts was used for expression-based analyses.

Enrichment of ISG$^+$ DC signature in Cheng et al. (Cell 2021)— Marker genes for the scRNA-seq-derived ISG$^+$ DC signature (Table S3) were translated from mouse to human symbols using the Broad GSEA chip file (MSigDB v7.2; https://data.broadinstitute.org/gsea-msigdb/msigdb/annotations_versioned/Mouse_Gene_Symbol_Remapping_Human_Orthologs_MSigDB.v7.2.chip) (Liberzon et al., 2011; Subramanian et al., 2005). First, all cells in the Cheng et al. dataset were scored with the translated marker gene list using the AddModuleScore (Tirosh et al., 2016) function in Seurat. Per-cluster enrichment for high-scoring cells and pairwise enrichment between clusters were assessed as described in the section below. Subsequently, tumor-only cells in our re-analysis of the Cheng et al. dataset were scored in a similar fashion and likewise tested for enrichment per cluster.

Statistical tests for enrichment of external signatures in scRNA-seq clusters— Related to Figures 3L, 3R, S3C, and S3D. Statistical significance for the enrichment of high-scoring cells (standardized module score: > 2 for bulk RNA-seq signatures, > 2.5 for ISG$^+$ DC scRNA-seq signature) was assessed using an upper-tailed hypergeometric test of proportions (phyper, Stats R package; alpha = 0.05). To compare signature module scores for all cells within a given cluster with cells in every other cluster in a pairwise fashion, a two-sided Wilcoxon rank sum test (wilcox.test, Stats R package; alpha = 0.05) was used.

Collection of tumor-conditioned media—Tumor-conditioned media was collected when flasks containing MC38-SIY, MC57-SIY, or MC57-SIY-*Irf3*$^{-/-}$ tumor cells reached 100% confluency. Tumor supernatant was centrifuged at 500 *g* for 3 min to pellet cell debris and subsequently filtered through a 0.45 μm PVDF syringe filter (EMD Millipore). The resultant cell-free tumor-conditioned media was aliquoted and stored at −20°C.

Generation of BM-DCs—Adapted from (Mayer et al., 2014). BM was harvested from the femur and tibia of mice by flushing the bones with RPMI using a 1 mL syringe. Cells were passed through a 70 μm filter, washed twice with PBS, and cultured at a density of 1.5×10^6 cells/mL in RPMI supplemented with 10% FBS, 1% penicillin/streptomycin, 1X HEPES, 1X MEM Non-Essential Amino Acids, 1X β-mercaptoethanol, 100 ng/mL recombinant human FLT3-L (Bio X Cell), and 5 ng/mL recombinant mouse GM-CSF (BioLegend) for 7 days at 37°C and 5% CO_2. BM-DCs at day 7 of culture were either used directly in assays or frozen in 10% DMSO in FBS and stored in liquid nitrogen.

BM-DC IFN-I and ISG induction assay—BM-DCs at day 7 of culture were plated at 3×10^6 cells per well of a 6-well tissue culture-treated plate and cultured with 2 mL of tumor-conditioned media. BM-DC were cultured with 2 mL of fresh complete DMEM

media as a negative control or with complete DMEM media containing 20 μg/mL DMXAA (InvivoGen) as a positive control. Following 24 hr incubation at 37°C and 5% CO_2, BM-DC were washed, lysed with RLT Buffer (QIAGEN), and frozen at −80°C for subsequent RNA extraction.

Baseline IFN-I and ISG screen with mouse and human tumor cell lines—Murine and human tumor cell lines used for the IFN-I and ISG qPCR screen were either available in-house, gifts, or purchased from ATCC or the High Throughput Sciences Core at the Koch Institute Swanson Biotechnology Center and cultured at the indicated conditions (Table S6). For the experiment, 3×10^5 cells were washed with PBS, lysed with RLT Buffer, and frozen at −80°C for subsequent RNA extraction.

RNA isolation, cDNA reaction, and qRT-PCR—RNA was isolated using the QIAGEN RNeasy Kit (QIAGEN) following manufacturer's instructions. Extracted RNA was quantified by NanoDrop and 500 ng of RNA was reverse transcribed into cDNA using the Applied Biosystems Reverse Transcriptase Kit, following manufacturer's instructions. For each qRT-PCR reaction, 1 μL of the cDNA was assayed using the Applied Biosystems SYBR Green PCR Master Mix with defined primer sets for each target gene (Table S5). Reactions were run on the StepOne Real-Time PCR System (Applied Biosystems) and the expression level was calculated as $2^{-\Delta CT}$, where ΔCT is the difference between the CT values of the target gene and 18S.

Protective systemic immunity assay—*Batf3*$^{-/-}$ mice were implanted subcutaneously in the flank with 2×10^6 MC57-SIY tumor cells or 2×10^6 MC57-SIY-*B2M*$^{-/-}$ tumor cells to induce the immune response by ISG$^+$ DC. As a control, a cohort of *Batf3*$^{-/-}$ mice was injected with equal volume of PBS. Six days after the initial implantation with MC57 tumor cells or PBS control, 2×10^6 MC38-SIY tumor cells were implanted on the contralateral flanks of the mice, and tumor outgrowth was measured as previously described.

QUANTIFICATION AND STATISTICAL ANALYSIS

All statistical analyses were performed using GraphPad Prism (GraphPad). All data are shown as mean ± s.e.m. Unless stated otherwise, statistical analyses were performed with MWU test (for comparison of two groups) or two-way ANOVA (for multiple comparisons) with *p < 0.05; **p < 0.01; ***p < 0.001; ****p < 0.0001; ns = not significant.

Supplementary Material

Refer to Web version on PubMed Central for supplementary material.

ACKNOWLEDGMENTS

We thank P. Sharp, T. Jacks, D. Irvine, and A. Amon for advice and review of the manuscript; J. Cyster (UCSF) and T. Mempel (Harvard/MGH) for providing zDC-DTR mice; R. Warner in the Mempel Lab for assistance with zDC-DTR BMC experiments; M. Duquette for mouse colony maintenance; and P. Thompson for administrative support. We thank the Koch Institute's Robert A. Swanson (1969) Biotechnology Center and the Whitehead Institute Genome Technology Core for providing core services. This work was supported by NIH cancer core grant P30 CA014051-49 and in part by the NIH pre-doctoral training grant T32GM007287, the David H. Koch Graduate

Fellowship, the Howard S. (1953) and Linda B. Stern Career Development Professorship, and the Pew-Stewart Scholarship.

REFERENCES

Albacker LA, Wu J, Smith P, Warmuth M, Stephens PJ, Zhu P, Yu L, and Chmielecki J. (2017). Loss of function JAK1 mutations occur at high frequency in cancers with microsatellite instability and are suggestive of immune evasion. PLoS ONE 12, e0176181.

Barry KC, Hsu J, Broz ML, Cueto FJ, Binnewies M, Combes AJ, Nelson AE, Loo K, Kumar R, Rosenblum MD, et al. (2018). A natural killer-dendritic cell axis defines checkpoint therapy-responsive tumor microenvironments. Nat. Med. 24, 1178–1191. [PubMed: 29942093]

Bidwell BN, Slaney CY, Withana NP, Forster S, Cao Y, Loi S, Andrews D, Mikeska T, Mangan NE, Samarajiwa SA, et al. (2012). Silencing of Irf7 pathways in breast cancer cells promotes bone metastasis through immune escape. Nat. Med. 18, 1224–1231. [PubMed: 22820642]

Bosteels C, Neyt K, Vanheerswynghels M, van Helden MJ, Sichien D, Debeuf N, De Prijck S, Bosteels V, Vandamme N, Martens L, et al. (2020). Inflammatory type 2 cDCs acquire features of cDC1s and macrophages to orchestrate immunity to respiratory virus infection. Immunity 52, 1039–1056.e9. [PubMed: 32392463]

Böttcher JP, Bonavita E, Chakravarty P, Blees H, Cabeza-Cabrerizo M, Sammicheli S, Rogers NC, Sahai E, Zelenay S, and Reis e Sousa C. (2018). NK cells stimulate recruitment of cDC1 into the tumor microenvironment promoting cancer immune control. Cell 172, 1022–1037.e14. [PubMed: 29429633]

Briseño CG, Haldar M, Kretzer NM, Wu X, Theisen DJ, Kc W, Durai V, Grajales-Reyes GE, Iwata A, Bagadia P, et al. (2016). Distinct transcriptional programs control cross-priming in classical and monocyte-derived dendritic cells. Cell Rep. 15, 2462–2474. [PubMed: 27264183]

Broz ML, Binnewies M, Boldajipour B, Nelson AE, Pollack JL, Erle DJ, Barczak A, Rosenblum MD, Daud A, Barber DL, et al. (2014). Dissecting the tumor myeloid compartment reveals rare activating antigen-presenting cells critical for T cell immunity. Cancer Cell 26, 638–652. [PubMed: 25446897]

Bullock TNJ, Mullins DW, and Engelhard VH (2003). Antigen density presented by dendritic cells in vivo differentially affects the number and avidity of primary, memory, and recall CD8+ T cells. J. Immunol. 170, 1822–1829. [PubMed: 12574347]

Burnette BC, Liang H, Lee Y, Chlewicki L, Khodarev NN, Weichselbaum RR, Fu YX, and Auh SL (2011). The efficacy of radiotherapy relies upon induction of type I interferon-dependent innate and adaptive immunity. Cancer Res. 71, 2488–2496. [PubMed: 21300764]

Butler A, Hoffman P, Smibert P, Papalexi E, and Satija R. (2018). Integrating single-cell transcriptomic data across different conditions, technologies, and species. Nat. Biotechnol. 36, 411–420. [PubMed: 29608179]

Chen DS, and Mellman I. (2013). Oncology meets immunology: The cancer-immunity cycle. Immunity 39, 1–10. [PubMed: 23890059]

Chen L, and Flies DB (2013). Molecular mechanisms of T cell co-stimulation and co-inhibition. Nat. Rev. Immunol. 13, 227–242. [PubMed: 23470321]

Cheng S, Li Z, Gao R, Xing B, Gao Y, Yang Y, Qin S, Zhang L, Ouyang H, Du P, et al. (2021). A pan-cancer single-cell transcriptional atlas of tumor infiltrating myeloid cells. Cell 184, 792–809.e23. [PubMed: 33545035]

Das Mohapatra A, Tirrell I, Bénéchet AP, Pattnayak S, Khanna KM, and Srivastava PK (2020). Cross-dressing of CD8α$^+$ dendritic cells with antigens from live mouse tumor cells is a major mechanism of cross-priming. Cancer Immunol. Res. 8, 1287–1299. [PubMed: 32759362]

den Haan JM, Lehar SM, and Bevan MJ (2000). CD8$^+$ but not CD8$^-$ dendritic cells cross-prime cytotoxic T cells in vivo. J. Exp. Med. 192, 1685–1696. [PubMed: 11120766]

Edelson BT, Kc W, Juang R, Kohyama M, Benoit LA, Klekotka PA, Moon C, Albring JC, Ise W, Michael DG, et al. (2010). Peripheral CD103$^+$ dendritic cells form a unified subset developmentally related to CD8α$^+$ conventional dendritic cells. J. Exp. Med. 207, 823–836. [PubMed: 20351058]

Eisenbarth SC (2019). Dendritic cell subsets in T cell programming: Location dictates function. Nat. Rev. Immunol. 19, 89–103. [PubMed: 30464294]

Embgenbroich M, and Burgdorf S. (2018). Current concepts of antigen cross-presentation. Front. Immunol. 9, 1643. [PubMed: 30061897]

Fridman WH, Pagès F, Sautès-Fridman C, and Galon J. (2012). The immune contexture in human tumours: Impact on clinical outcome. Nat. Rev. Cancer 12, 298–306. [PubMed: 22419253]

Fuertes MB, Woo SR, Burnett B, Fu YX, and Gajewski TF (2013). Type I interferon response and innate immune sensing of cancer. Trends Immunol. 34, 67–73. [PubMed: 23122052]

Gao Y, Nish SA, Jiang R, Hou L, Licona-Limón P, Weinstein JS, Zhao H, and Medzhitov R. (2013). Control of T helper 2 responses by transcription factor IRF4-dependent dendritic cells. Immunity 39, 722–732. [PubMed: 24076050]

Gerhard GM, Bill R, Messemaker M, Klein AM, and Pittet MJ (2021). Tumor-infiltrating dendritic cell states are conserved across solid human cancers. J. Exp. Med. 218, e20200264.

Guilliams M, Dutertre C-A, Scott CL, McGovern N, Sichien D, Chakarov S, Van Gassen S, Chen J, Poidinger M, De Prijck S, et al. (2016). Unsupervised high-dimensional analysis aligns dendritic cells across tissues and species. Immunity 45, 669–684. [PubMed: 27637149]

Guilliams M, Ginhoux F, Jakubzick C, Naik SH, Onai N, Schraml BU, Segura E, Tussiwand R, and Yona S. (2014). Dendritic cells, monocytes and macrophages: A unified nomenclature based on ontogeny. Nat. Rev. Immunol. 14, 571–578. [PubMed: 25033907]

Heidegger I, Pircher A, and Pichler R. (2019). Targeting the tumor microenvironment in renal cell cancer biology and therapy. Front. Oncol. 9, 490. [PubMed: 31259150]

Hervas-Stubbs S, Perez-Gracia JL, Rouzaut A, Sanmamed MF, Le Bon A, and Melero I. (2011). Direct effects of type I interferons on cells of the immune system. Clin. Cancer Res. 17, 2619–2627. [PubMed: 21372217]

Hildner K, Edelson BT, Purtha WE, Diamond M, Matsushita H, Kohyama M, Calderon B, Schraml BU, Unanue ER, Diamond MS, et al. (2008). Batf3 deficiency reveals a critical role for $CD8\alpha^+$ dendritic cells in cytotoxic T cell immunity. Science 322, 1097–1100. [PubMed: 19008445]

Huber JP, and Farrar JD (2011). Regulation of effector and memory T-cell functions by type I interferon. Immunology 132, 466–474. [PubMed: 21320124]

Inaba K, Young JW, and Steinman RM (1987). Direct activation of $CD8^+$ cytotoxic T lymphocytes by dendritic cells. J. Exp. Med. 166, 182–194. [PubMed: 2955069]

Ishizuka JJ, Manguso RT, Cheruiyot CK, Bi K, Panda A, Iracheta-Vellve A, Miller BC, Du PP, Yates KB, Dubrot J, et al. (2019). Loss of ADAR1 in tumours overcomes resistance to immune checkpoint blockade. Nature 565, 43–48. [PubMed: 30559380]

Iurescia S, Fioretti D, and Rinaldi M. (2020). The innate immune signalling pathways: turning RIG-I sensor activation against cancer. Cancers (Basel) 12, 3158. [PubMed: 33121210]

Iyoda T, Shimoyama S, Liu K, Omatsu Y, Akiyama Y, Maeda Y, Takahara K, Steinman RM, and Inaba K. (2002). The $CD8^+$ dendritic cell subset selectively endocytoses dying cells in culture and in vivo. J. Exp. Med. 195, 1289–1302. [PubMed: 12021309]

Kalbasi A, and Ribas A. (2020). Tumour-intrinsic resistance to immune checkpoint blockade. Nat. Rev. Immunol. 20, 25–39. [PubMed: 31570880]

Katlinskaya YV, Katlinski KV, Yu Q, Ortiz A, Beiting DP, Brice A, Davar D, Sanders C, Kirkwood JM, Rui H, et al. (2016). Suppression of type I interferon signaling overcomes oncogene-induced senescence and mediates melanoma development and progression. Cell Rep. 15, 171–180. [PubMed: 27052162]

Katlinski KV, Gui J, Katlinskaya YV, Ortiz A, Chakraborty R, Bhattacharya S, Carbone CJ, Beiting DP, Girondo MA, Peck AR, et al. (2017). Inactivation of interferon receptor promotes the establishment of immune privileged tumor microenvironment. Cancer Cell 31, 194–207. [PubMed: 28196594]

Krishnaswamy JK, Gowthaman U, Zhang B, Mattsson J, Szeponik L, Liu D, Wu R, White T, Calabro S, Xu L, et al. (2017). Migratory CD11b+ conventional dendritic cells induce T follicular helper cell-dependent antibody responses. Sci. Immunol 2, eaam9169.

Langmead B, Trapnell C, Pop M, and Salzberg SL (2009). Ultrafast and memory-efficient alignment of short DNA sequences to the human genome. Genome Biol. 10, R25. [PubMed: 19261174]

Laoui D, Keirsse J, Morias Y, Van Overmeire E, Geeraerts X, Elkrim Y, Kiss M, Bolli E, Lahmar Q, Sichien D, et al. (2016). The tumour microenvironment harbours ontogenically distinct dendritic cell populations with opposing effects on tumour immunity. Nat. Commun. 7, 13720. [PubMed: 28008905]

Le Naour J, Zitvogel L, Galluzzi L, Vacchelli E, and Kroemer G. (2020). Trial watch: STING agonists in cancer therapy. OncoImmunology 9, 1777624–1777624.

Lenschow DJ, Walunas TL, and Bluestone JA (1996). CD28/B7 system of T cell costimulation. Annu. Rev. Immunol. 14, 233–258. [PubMed: 8717514]

León B, López-Bravo M, and Ardavíń C. (2007). Monocyte-derived dendritic cells formed at the infection site control the induction of protective T helper 1 responses against Leishmania. Immunity 26, 519–531. [PubMed: 17412618]

Li B, and Dewey CN (2011). RSEM: Accurate transcript quantification from RNA-seq data with or without a reference genome. BMC Bioinformatics 12, 323. [PubMed: 21816040]

Liberzon A, Subramanian A, Pinchback R, Thorvaldsdóttir H, Tamayo P, and Mesirov JP (2011). Molecular signatures database (MSigDB) 3.0. Bioinformatics 27, 1739–1740. [PubMed: 21546393]

Linsley PS, Speake C, Whalen E, and Chaussabel D. (2014). Copy number loss of the interferon gene cluster in melanomas is linked to reduced T cell infiltrate and poor patient prognosis. PLoS ONE 9, e109760. [PubMed: 25314013]

Liu H, Golji J, Brodeur LK, Chung FS, Chen JT, deBeaumont RS, Bullock CP, Jones MD, Kerr G, Li L, et al. (2019). Tumor-derived IFN triggers chronic pathway agonism and sensitivity to ADAR loss. Nat. Med. 25, 95–102. [PubMed: 30559422]

Liu X, Liu L, Ren Z, Yang K, Xu H, Luan Y, Fu K, Guo J, Peng H, Zhu M, and Fu YX (2018). Dual targeting of innate and adaptive checkpoints on tumor cells limits immune evasion. Cell Rep. 24, 2101–2111. [PubMed: 30134171]

Love MI, Huber W, and Anders S. (2014). Moderated estimation of fold change and dispersion for RNA-seq data with DESeq2. Genome Biol. 15, 550. [PubMed: 25516281]

Ma Y, Adjemian S, Mattarollo SR, Yamazaki T, Aymeric L, Yang H, Portela Catani JP, Hannani D, Duret H, Steegh K, et al. (2013). Anticancer chemotherapy-induced intratumoral recruitment and differentiation of antigen-presenting cells. Immunity 38, 729–741. [PubMed: 23562161]

Maier B, Leader AM, Chen ST, Tung N, Chang C, LeBerichel J, Chudnovskiy A, Maskey S, Walker L, Finnigan JP, et al. (2020). A conserved dendritic-cell regulatory program limits antitumour immunity. Nature 580, 257–262. [PubMed: 32269339]

Mayer CT, Ghorbani P, Nandan A, Dudek M, Arnold-Schrauf C, Hesse C, Berod L, Stüve P, Puttur F, Merad M, and Sparwasser T. (2014). Selective and efficient generation of functional Batf3-dependent CD103^{+} dendritic cells from mouse bone marrow. Blood 124, 3081–3091. [PubMed: 25100743]

Menezes S, Melandri D, Anselmi G, Perchet T, Loschko J, Dubrot J, Patel R, Gautier EL, Hugues S, Longhi MP, et al. (2016). The heterogeneity of Ly6C^{hi} monocytes controls their differentiation into iNOS^{+} macrophages or monocyte-derived dendritic cells. Immunity 45, 1205–1218. [PubMed: 28002729]

Merad M, Sathe P, Helft J, Miller J, and Mortha A. (2013). The dendritic cell lineage: Ontogeny and function of dendritic cells and their subsets in the steady state and the inflamed setting. Annu. Rev. Immunol. 31, 563–604. [PubMed: 23516985]

Meredith MM, Liu K, Darrasse-Jeze G, Kamphorst AO, Schreiber HA, Guermonprez P, Idoyaga J, Cheong C, Yao K-H, Niec RE, and Nussenzweig MC (2012). Expression of the zinc finger transcription factor zDC (Zbtb46, Btbd4) defines the classical dendritic cell lineage. J. Exp. Med. 209, 1153–1165. [PubMed: 22615130]

Michea P, Noe€l F, Zakine E, Czerwinska U, Sirven P, Abouzid O, Goudot C, Scholer-Dahirel A, Vincent-Salomon A, Reyal F, et al. (2018). Adjustment of dendritic cells to the breast-cancer microenvironment is subset specific. Nat. Immunol. 19, 885–897. [PubMed: 30013147]

Mildner A, and Jung S. (2014). Development and function of dendritic cell subsets. Immunity 40, 642–656. [PubMed: 24837101]

Mootha VK, Lindgren CM, Eriksson K-F, Subramanian A, Sihag S, Lehar J, Puigserver P, Carlsson E, Ridderstrå le M, Laurila E, et al. (2003). PGC-1α-responsive genes involved in oxidative phosphorylation are coordinately downregulated in human diabetes. Nat. Genet. 34, 267–273. [PubMed: 12808457]

Mumberg D, Monach PA, Wanderling S, Philip M, Toledano AY, Schreiber RD, and Schreiber H. (1999). $CD4^+$ T cells eliminate MHC class II-negative cancer cells in vivo by indirect effects of IFN-γ. Proc. Natl. Acad. Sci. USA 96, 8633–8638. [PubMed: 10411927]

Murphy TL, Grajales-Reyes GE, Wu X, Tussiwand R, Briseño CG, Iwata A, Kretzer NM, Durai V, and Murphy KM (2016). Transcriptional control of dendritic cell development. Annu. Rev. Immunol. 34, 93–119. [PubMed: 26735697]

Musella M, Manic G, De Maria R, Vitale I, and Sistigu A. (2017). Type-I-interferons in infection and cancer: Unanticipated dynamics with therapeutic implications. OncoImmunology 6, e1314424.

Nakayama M, Hori A, Toyoura S, and Yamaguchi S-I (2021). Shaping of T cell functions by trogocytosis. Cells 10, 1155. [PubMed: 34068819]

Nguyen KB, and Spranger S. (2020). Modulation of the immune microenvironment by tumor-intrinsic oncogenic signaling. J. Cell Biol. 219, e201908224. [PubMed: 31816057]

Porgador A, Yewdell JW, Deng Y, Bennink JR, and Germain RN (1997). Localization, quantitation, and in situ detection of specific peptide-MHC class I complexes using a monoclonal antibody. Immunity 6, 715–726. [PubMed: 9208844]

Raval A, Puri N, Rath PC, and Saxena RK (1998). Cytokine regulation of expression of class I MHC antigens. Exp. Mol. Med. 30, 1–13. [PubMed: 9873816]

Roberts EW, Broz ML, Binnewies M, Headley MB, Nelson AE, Wolf DM, Kaisho T, Bogunovic D, Bhardwaj N, and Krummel MF (2016).Critical role for CD103+/CD141+ dendritic cells bearing CCR7 for tumor antigen trafficking and priming of T cell immunity in melanoma. Cancer Cell 30, 324–336. [PubMed: 27424807]

Salmon H, Idoyaga J, Rahman A, Leboeuf M, Remark R, Jordan S, Casanova-Acebes M, Khudoynazarova M, Agudo J, Tung N, et al. (2016). Expansion and activation of $CD103^+$ dendritic cell progenitors at the tumor site enhances tumor responses to therapeutic PD-L1 and BRAF inhibition. Immunity 44, 924–938. [PubMed: 27096321]

Sancho D, Joffre OP, Keller AM, Rogers NC, Martínez D, Hernanz-Falcón P, Rosewell I, and Reis e Sousa C. (2009). Identification of a dendritic cell receptor that couples sensing of necrosis to immunity. Nature 458, 899–903. [PubMed: 19219027]

Sancho D, Mourão-Sá D, Joffre OP, Schulz O, Rogers NC, Pennington DJ, Carlyle JR, and Reis e Sousa C. (2008). Tumor therapy in mice via antigen targeting to a novel, DC-restricted C-type lectin. J. Clin. Invest. 118, 2098–2110. [PubMed: 18497879]

Sato M, Suemori H, Hata N, Asagiri M, Ogasawara K, Nakao K, Nakaya T, Katsuki M, Noguchi S, Tanaka N, and Taniguchi T. (2000). Distinct and essential roles of transcription factors IRF-3 and IRF-7 in response to viruses for IFN-α/β gene induction. Immunity 13, 539–548. [PubMed: 11070172]

Schadt L, Sparano C, Schweiger NA, Silina K, Cecconi V, Lucchiari G, Yagita H, Guggisberg E, Saba S, Nascakova Z, et al. (2019). Cancer-cell-intrinsic cGAS expression mediates tumor immunogenicity. Cell Rep. 29, 1236–1248.e7. [PubMed: 31665636]

Schmid ET, Pang IK, Carrera Silva EA, Bosurgi L, Miner JJ, Diamond MS, Iwasaki A, and Rothlin CV (2016). AXL receptor tyrosine kinase is required for T cell priming and antiviral immunity. eLife 5, e12414. [PubMed: 27350258]

Schulz O, and Reis e Sousa C. (2002). Cross-presentation of cell-associated antigens by $CD8α^+$ dendritic cells is attributable to their ability to internalize dead cells. Immunology 107, 183–189. [PubMed: 12383197]

Serbina NV, Salazar-Mather TP, Biron CA, Kuziel WA, and Pamer EG (2003). TNF/iNOS-producing dendritic cells mediate innate immune defense against bacterial infection. Immunity 19, 59–70. [PubMed: 12871639]

Sharma MD, Rodriguez PC, Koehn BH, Baban B, Cui Y, Guo G, Shimoda M, Pacholczyk R, Shi H, Lee EJ, et al. (2018). Activation of p53 in immature myeloid precursor cells controls

differentiation into Ly6c^{+}CD103^{+} monocytic antigen-presenting cells in tumors. Immunity 48, 91–106.e6. [PubMed: 29343444]

Sistigu A, Yamazaki T, Vacchelli E, Chaba K, Enot DP, Adam J, Vitale I, Goubar A, Baracco EE, Remédios C, et al. (2014). Cancer cell-autonomous contribution of type I interferon signaling to the efficacy of chemotherapy. Nat. Med. 20, 1301–1309. [PubMed: 25344738]

Spranger S, Bao R, and Gajewski TF (2015). Melanoma-intrinsic b-catenin signalling prevents anti-tumour immunity. Nature 523, 231–235. [PubMed: 25970248]

Spranger S, Dai D, Horton B, and Gajewski TF (2017). Tumor-residing Batf3 dendritic cells are required for effector T cell trafficking and adoptive T cell therapy. Cancer Cell 31, 711–723.e4. [PubMed: 28486109]

Spranger S, and Gajewski TF (2018). Mechanisms of tumor cell-intrinsic immune evasion. Annu. Rev. Cancer Biol. 2, 213–228.

Squadrito ML, Cianciaruso C, Hansen SK, and De Palma M. (2018). EVIR: Chimeric receptors that enhance dendritic cell cross-dressing with tumor antigens. Nat. Methods 15, 183–186. [PubMed: 29355847]

Stuart T, Butler A, Hoffman P, Hafemeister C, Papalexi E, Mauck WM 3rd, Hao Y, Stoeckius M, Smibert P, and Satija R. (2019). Comprehensive integration of single-cell data. Cell 177, 1888–1902.e21. [PubMed: 31178118]

Subramanian A, Tamayo P, Mootha VK, Mukherjee S, Ebert BL, Gillette MA, Paulovich A, Pomeroy SL, Golub TR, Lander ES, and Mesirov JP (2005). Gene set enrichment analysis: A knowledge-based approach for interpreting genome-wide expression profiles. Proc. Natl. Acad. Sci. USA 102, 15545–15550. [PubMed: 16199517]

Subramanian M, Hayes CD, Thome JJ, Thorp E, Matsushima GK, Herz J, Farber DL, Liu K, Lakshmana M, and Tabas I. (2014). An AXL/LRP-1/RANBP9 complex mediates DC efferocytosis and antigen cross-presentation in vivo. J. Clin. Invest. 124, 1296–1308. [PubMed: 24509082]

Sykulev Y, Anikeeva N, and Gakamsky D. (2012). The role of peptide-MHC ligand density in stimulating T-cell receptor signaling. J. Immunol. 188 (1 Suppl) 58.21.

Takahashi M, Lio CJ, Campeau A, Steger M, Ay F, Mann M, Gonzalez DJ, Jain M, and Sharma S. (2021). The tumor suppressor kinase DAPK3 drives tumor-intrinsic immunity through the STING-IFN-β pathway. Nat. Immunol. 22, 485–496. [PubMed: 33767426]

Tamura T, Tailor P, Yamaoka K, Kong HJ, Tsujimura H, O'Shea JJ, Singh H, and Ozato K. (2005). IFN regulatory factor-4 and −8 govern dendritic cell subset development and their functional diversity. J. Immunol. 174, 2573–2581. [PubMed: 15728463]

Tamura T, Yanai H, Savitsky D, and Taniguchi T. (2008). The IRF family transcription factors in immunity and oncogenesis. Annu. Rev. Immunol. 26, 535–584. [PubMed: 18303999]

Tirosh I, Izar B, Prakadan SM, Wadsworth MH 2nd, Treacy D, Trombetta JJ, Rotem A, Rodman C, Lian C, Murphy G, et al. (2016). Dissecting the multicellular ecosystem of metastatic melanoma by single-cell RNA-seq. Science 352, 189–196. [PubMed: 27124452]

Trujillo JA, Sweis RF, Bao R, and Luke JJ (2018). T cell-inflamed versus non-T cell-inflamed tumors: A conceptual framework for cancer immunotherapy drug development and combination therapy selection. Cancer Immunol. Res. 6, 990–1000. [PubMed: 30181337]

Tussiwand R, Everts B, Grajales-Reyes GE, Kretzer NM, Iwata A, Bagaitkar J, Wu X, Wong R, Anderson DA, Murphy TL, et al. (2015). Klf4 expression in conventional dendritic cells is required for T helper 2 cell responses. Immunity 42, 916–928. [PubMed: 25992862]

Wakim LM, and Bevan MJ (2011). Cross-dressed dendritic cells drive memory CD8^{+} T-cell activation after viral infection. Nature 471, 629–632. [PubMed: 21455179]

Williams JW, Tjota MY, Clay BS, Vander Lugt B, Bandukwala HS, Hrusch CL, Decker DC, Blaine KM, Fixsen BR, Singh H, et al. (2013). Transcription factor IRF4 drives dendritic cells to promote Th2 differentiation. Nat. Commun. 4, 2990. [PubMed: 24356538]

Woo SR, Fuertes MB, Corrales L, Spranger S, Furdyna MJ, Leung MY, Duggan R, Wang Y, Barber GN, Fitzgerald KA, et al. (2014). STING-dependent cytosolic DNA sensing mediates innate immune recognition of immunogenic tumors. Immunity 41, 830–842. [PubMed: 25517615]

Yang L, Li A, Lei Q, and Zhang Y. (2019). Tumor-intrinsic signaling pathways: Key roles in the regulation of the immunosuppressive tumor microenvironment. J. Hematol. Oncol. 12, 125. [PubMed: 31775797]

Zaretsky JM, Garcia-Diaz A, Shin DS, Escuin-Ordinas H, Hugo W, Hu-Lieskovan S, Torrejon DY, Abril-Rodriguez G, Sandoval S, Barthly L, et al. (2016). Mutations associated with acquired resistance to PD-1 blockade in melanoma. N. Engl. J. Med. 375, 819–829. [PubMed: 27433843]

Zelenay S, Keller AM, Whitney PG, Schraml BU, Deddouche S, Rogers NC, Schulz O, Sancho D, and Reis e Sousa C. (2012). The dendritic cell receptor DNGR-1 controls endocytic handling of necrotic cell antigens to favor cross-priming of CTLs in virus-infected mice. J. Clin. Invest. 122, 1615–1627. [PubMed: 22505458]

Zhang JG, Czabotar PE, Policheni AN, Caminschi I, Wan SS, Kitsoulis S, Tullett KM, Robin AY, Brammananth R, van Delft MF, et al. (2012). The dendritic cell receptor Clec9A binds damaged cells via exposed actin filaments. Immunity 36, 646–657. [PubMed: 22483802]

Zilionis R, Engblom C, Pfirschke C, Savova V, Zemmour D, Saatcioglu HD, Krishnan I, Maroni G, Meyerovitz CV, Kerwin CM, et al. (2019). Single-cell transcriptomics of human and mouse lung cancers reveals conserved myeloid populations across individuals and species. Immunity 50, 1317–1334.e10. [PubMed: 30979687]

Zitvogel L, Galluzzi L, Kepp O, Smyth MJ, and Kroemer G. (2015). Type I interferons in anticancer immunity. Nat. Rev. Immunol. 15, 405–414. [PubMed: 26027717]

Highlights

- IFN-I induces a stimulatory DC2 state (ISG$^+$ DCs) that activates CD8$^+$ T cells
- *B2M*$^{-/-}$ ISG$^+$ DCs acquire and present tumor-derived pMHC class I complexes
- Precluding MHC class I transfer to ISG DCs ablates T cell responses in *Batf3*$^{-/-}$ mice
- ISG DCs can be induced by exogenous IFN-β addition to drive anti-tumor immunity

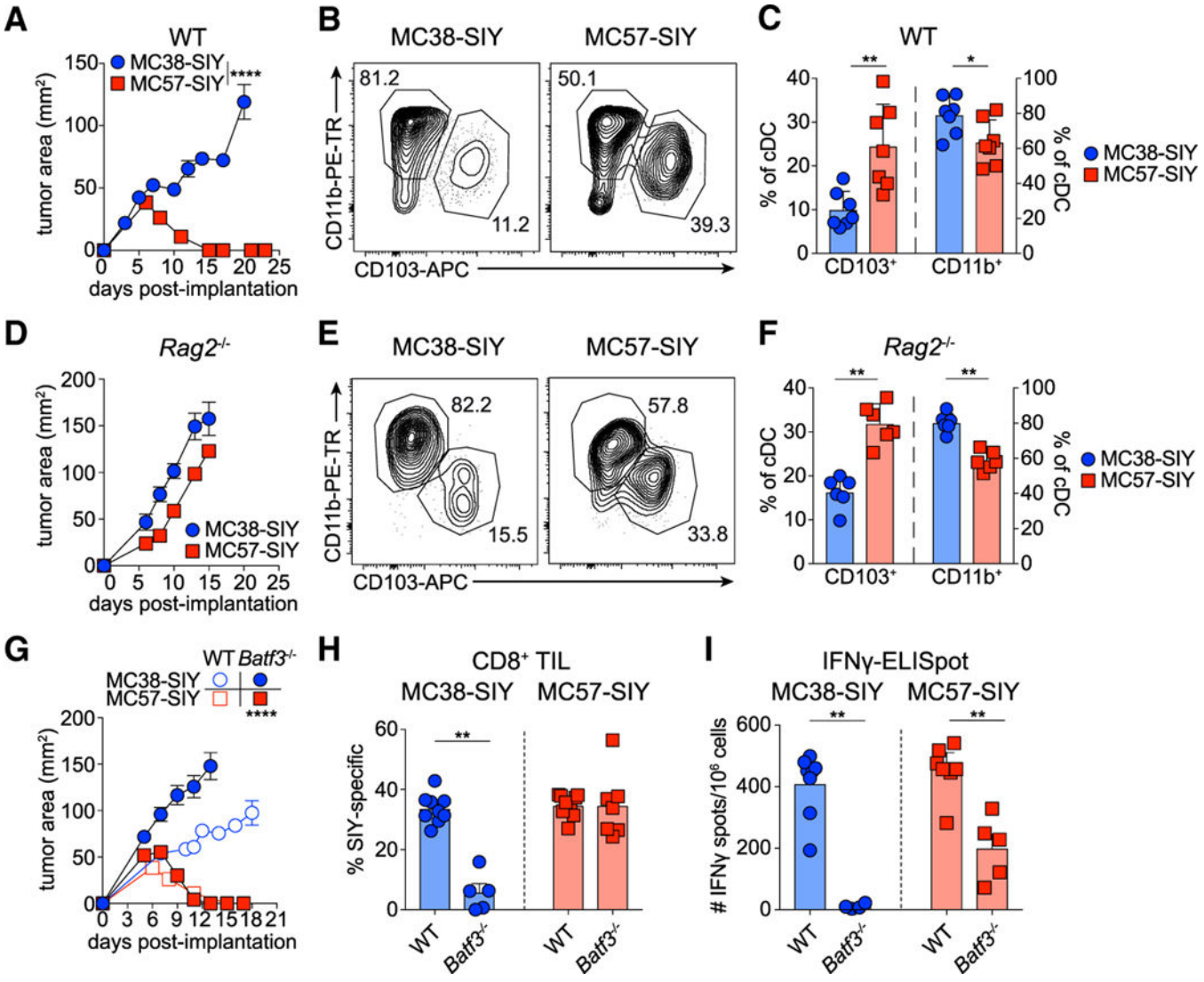

Figure 1. The regression of MC57-SIY tumors is independent of Batf3-driven DC1

(A) Representative tumor outgrowth in WT mice (n = 3–4 mice/group; three independent repeats).

(B and C) Representative flow plot (B) and quantification (C) of $CD103^+$ DC1s and $CD11b^+$ DC2s (pre-gated on live $CD45^+$MHC class $II^+Ly6C^-F4/80^-CD11c^+CD24^{hi}$) in tumors at day 7 after tumor inoculation in WT mice. Data were pooled from two independent experiments (n = 3–4 mice/group).

(D) Representative tumor outgrowth in *Rag2*$^{-/-}$ mice (n = 3–5 mice/group; three independent repeats). (E and F) Representative flow plot (E) and quantification (F) of $CD103^+$ DC1s and $CD11b^+$ DC2s in tumors at day 15 after tumor inoculation in *Rag2*$^{-/-}$ mice. Data were pooled from two independent experiments (n = 3 mice/group).

(G) Representative tumor outgrowth in WT or *Batf3*$^{-/-}$ mice (n = 3–4 mice/group; three independent repeats).

(H) Quantification of SIY-specific $CD8^+$ T cells in tumors at day 7 after tumor implantation in *Batf3*$^{-/-}$ mice. Data were pooled from two independent experiments (n = 2–5 mice mice/group).

(I) ELISpot quantification of IFN-γ-producing splenocytes at day 5 after tumor inoculation in WT and *Batf3*$^{-/-}$ mice. Data were pooled from two independent experiments (n = 3–4 mice/group).

Data are shown as mean ± SEM. *p < 0.05, **p < 0.01, ****p < 0.0001; ns, not significant: Mann-Whitney U (MWU) test (C, F, H, and I) or two-way ANOVA (A, D, and G).

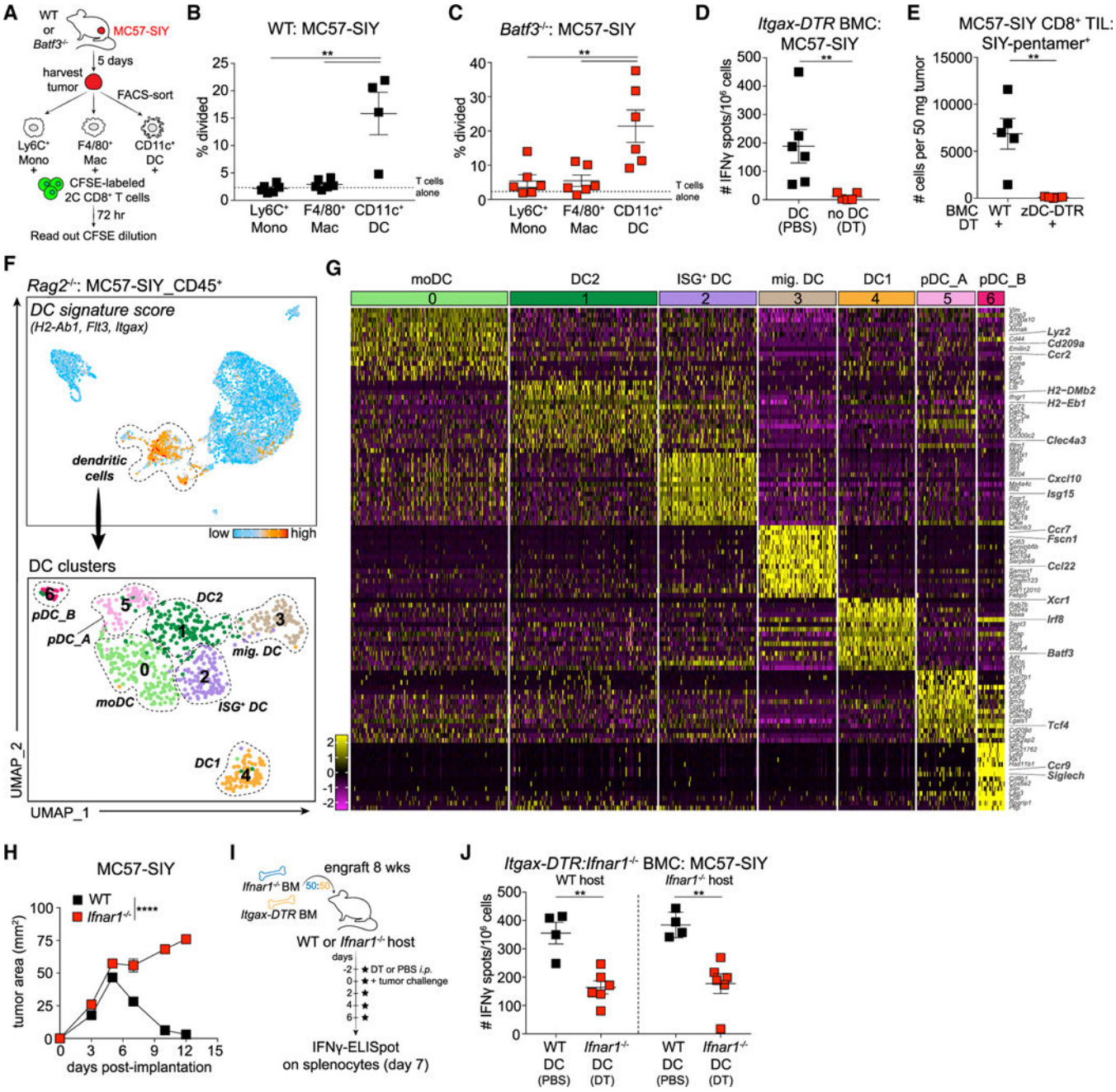

Figure 2. Functional assays and scRNA-seq identify a DC cluster characterized by an IFN-I gene signature in MC57-SIY tumors

(A) Experimental design for (B) and (C).

(B and C) Percentage of 2C T cell proliferation after co-culture with tumor-sorted APCs in WT (B) or *Batf3*$^{-/-}$ (C) mice at day 5 after tumor inoculation (n = 5 mice/experiment; two independent repeats).

(D) ELISpot of IFN-γ-producing splenocytes from DT-treated or PBS-treated *Itgax-DTR* BMC mice at day 5 after tumor inoculation. Data were pooled from two independent experiments (n = 3 mice/group).

(E) Number of SIY-reactive tumor-infiltrating lymphocytes (TILs) in tumors from cDC-depleted (zDC-DTR) or non-depleted (WT) BMC mice at day 7 after tumor inoculation (n = 5 mice/group).
(F) (Top) UMAP plot of cells from MC57-SIY tumors colored by expression module score of a DC signature. (Bottom) UMAP plot of cells contained in the highlighted DC cluster.
(G) Heatmap of top 15 DEGs for each DC cluster identified in (F).
(H) Tumor outgrowth (mm^2) in WT or *Ifnar1*$^{-/-}$ mice (n = 3–4 mice/group; three independent experiments).
(I) Experimental design for (J).
(J) ELISpot of IFN-γ-producing splenocytes from *Itgax-DTR:Ifnar1*$^{-/-}$ mixed BMC mice (WT hosts, left; *Ifnar1*$^{-/-}$ hosts, right) at day 7 after tumor inoculation. Data were pooled from two independent experiments (n = 2–3 mice/group).
Data are shown as mean ± SEM. **p < 0.01, ****p < 0.0001: MWU test (B–E and J) or two-way ANOVA (H).

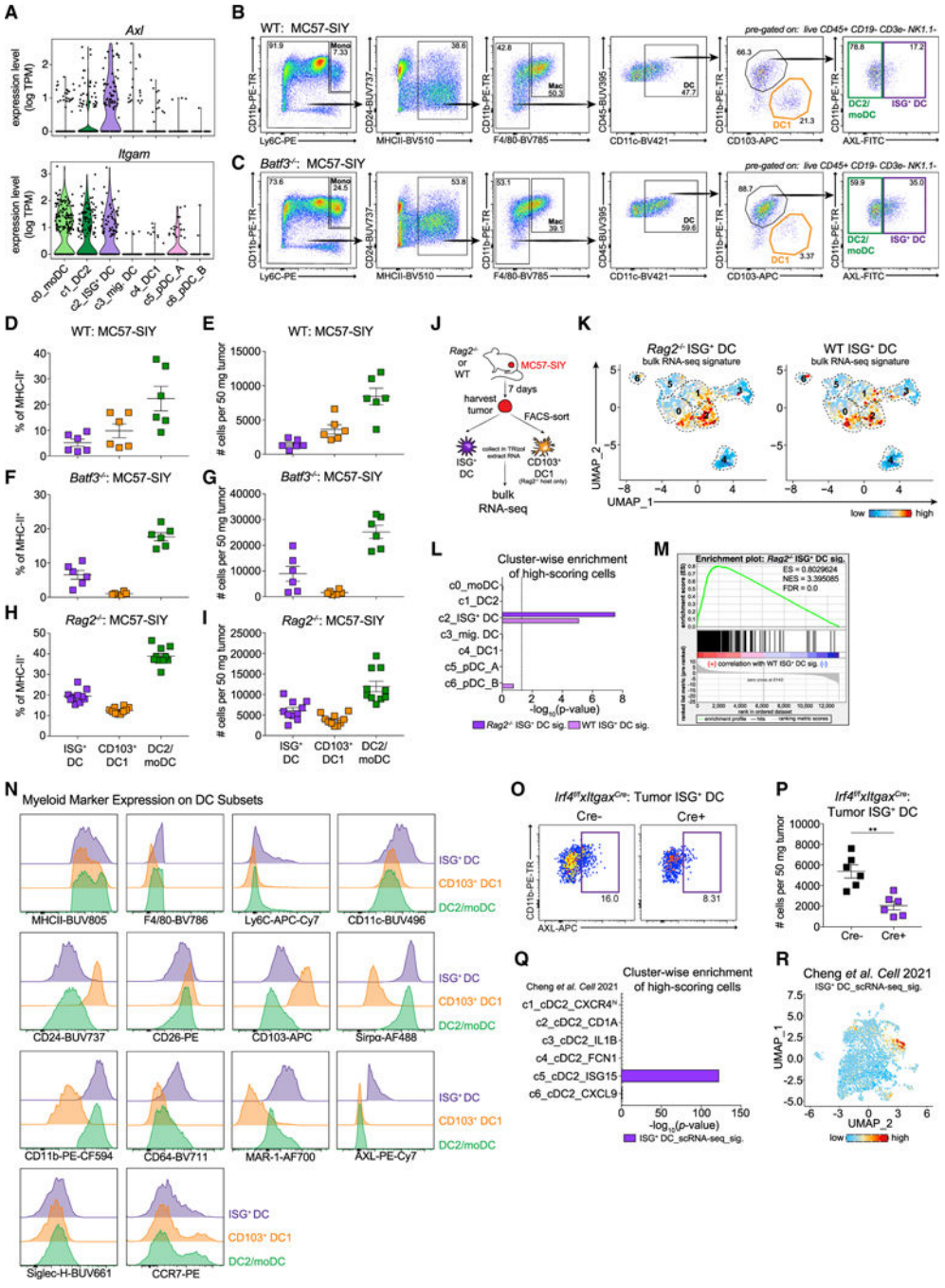

Figure 3. ISG$^+$ DCs are present in *Batf3*$^{-/-}$ mice and comprise an activation state of CD11b$^+$ DCs

(A) Violin plots of expression in DC clusters.

(B and C) Flow gating strategy for APCs and DCs in WT (B) or *Batf3*$^{-/-}$ (C) mice, pre-gated on live CD45$^+$CD19$^-$CD3e$^-$NK1.1$^-$ cells.

(D–I) Quantification of DC subsets in tumors from WT (D and E) and *Batf3*$^{-/-}$ (F and G) mice at day 7 after tumor inoculation, and in *Rag2*$^{-/-}$ mice (H and I) at day 11 after tumor inoculation. Data were pooled from two independent experiments (n = 3–5 mice/group).

(J) Experimental design for (K)–(M) and Figures S3B–S3D.

(K) Feature UMAP plots of DC clusters. Each cell is colored by an expression module score.
(L) Cluster-wise enrichment of cells scoring for the indicated bulk RNA-seq ISG^+ DC signatures. Dotted line denotes significance threshold (p = 0.05, hypergeometric test).
(M) GSEA plot showing highly significant enrichment of $Rag2^{-/-}$ ISG^+ DC signature in WT ISG^+ DC signature. ES, enrichment score; NES, normalized enrichment score; FDR, false discovery rate.
For (K)–(M), data are from two independent experiments (n = 5 mice/group).
(N) Representative histograms showing myeloid marker expression on DC subsets in tumors at day 7 post-implantation in WT mice (n = 3 mice/group; two independent repeats).
(O and P) Representative flow plot (O) and absolute numbers (P) of ISG^+ DCs at day 7 after tumor implantation in $Irf4^{f/f}xItgax^{Cre}$ or littermate control mice (n = 4–6 mice/group; two independent experiments).
(Q) Cluster-wise enrichment of cells that scored highly for the scRNA-seq-derived ISG^+ DC signature. Dotted line denotes significance threshold (p = 0.05, hypergeometric test).
(R) UMAP plot of human tumor-infiltrating DC2 subsets. Each cell is colored by its expression module score of the ISG^+ DC signature. Data are shown as mean ± SEM. **p < 0.01; MWU test (P).

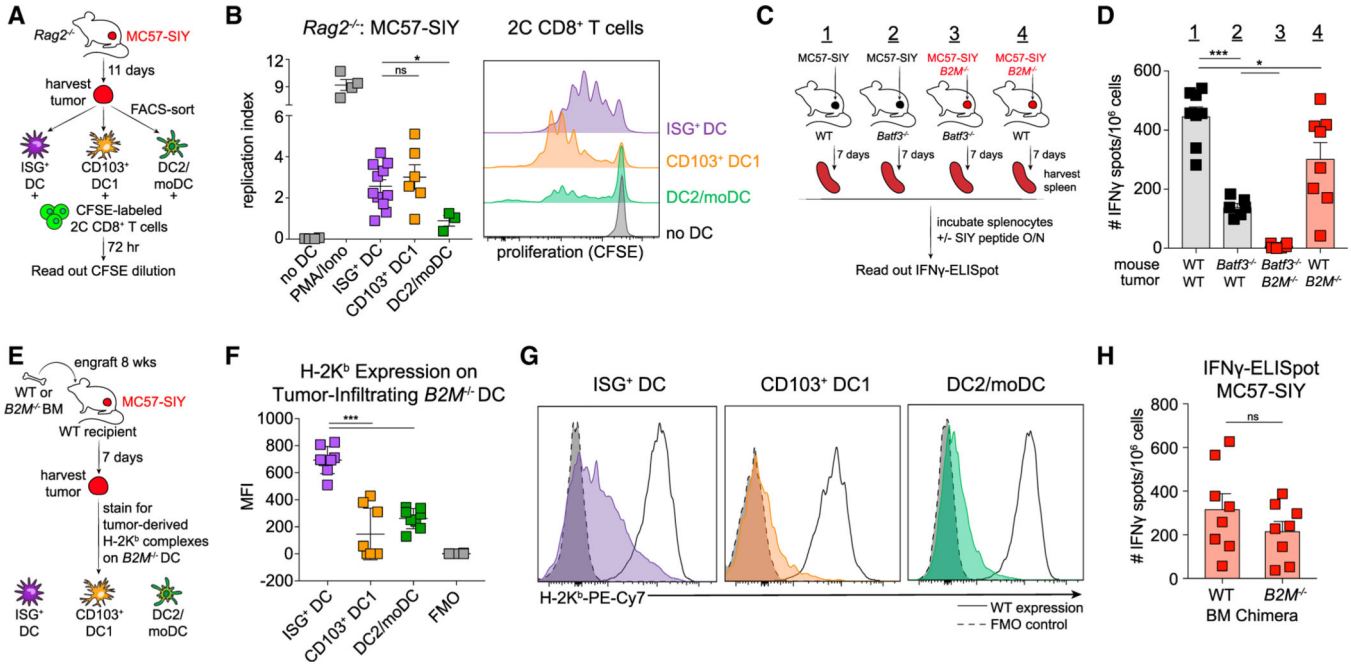

Figure 4. ISG$^+$ DCs acquire and present tumor antigens by MHC class I dressing

(A) Experimental design for (B).

(B) (Left) Replication index of 2C T cells after co-culture with tumor-sorted DCs from *Rag2*$^{-/-}$ mice at day 11 after tumor inoculation. Data were pooled from three independent experiments (n = 5 mice/experiment). (Right) Representative histogram.

(C) Experimental design for (D).

(D) ELISpot quantification of IFN-γ-producing splenocytes at day 7 after tumor inoculation in WT or *Batf3*$^{-/-}$ mice. Data were pooled from three independent experiments (n = 3–4 mice/group).

(E) Experimental design for (F) and (G).

(F and G) Quantification (F) and representative histograms (G) of H-2K^b expression on DC subsets infiltrating tumors in WT or *B2M*$^{-/-}$ BMC mice.

(H) ELISpot of IFN-γ-producing splenocytes from WT or *B2M*$^{-/-}$ BMC mice at day 7 after tumor inoculation.

For (F) and (H), data were pooled from two independent experiments (n = 4 mice/group). Data are shown as mean ± SEM. *p < 0.05, ***p < 0.001; ns, not significant: MWU test (B, D, F, and H).

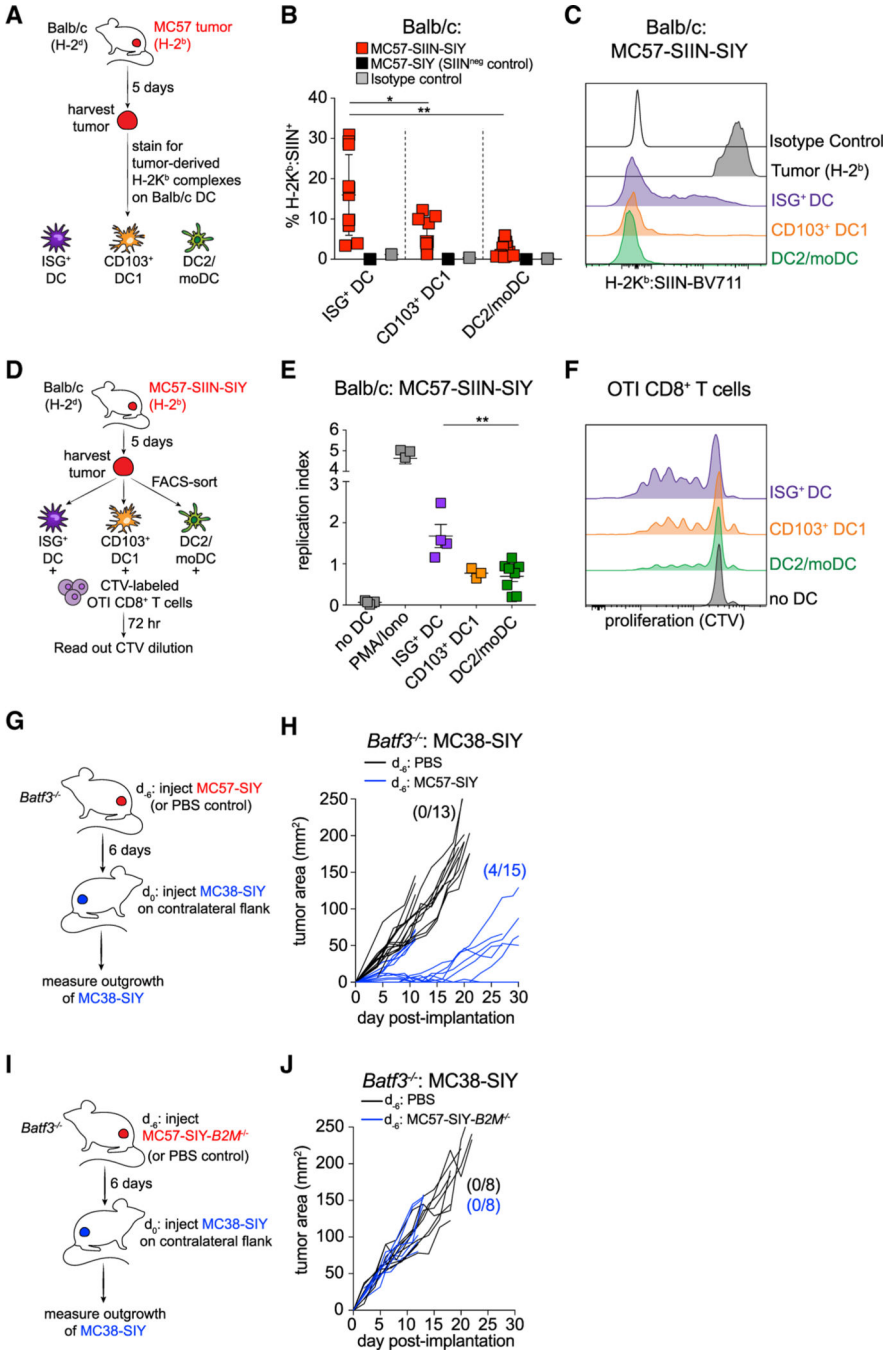

Figure 5. MHC class I-dressed ISG$^+$ DCs can induce protective systemic anti-tumor T cell immunity

(A) Experimental design for (B) and (C).

(B and C) Percentage (B) and representative histogram (C) of H-2K^b:SIIN expression on DC subsets in BALB/c mice at day 5 after tumor implantation. Data were pooled from three independent experiments (n = 3–4 mice/experiment).

(D) Experimental design for (E) and (F).

(E and F) Replication index (E) and representative histogram (F) of 2C T cell proliferation after co-culture with tumor-sorted DCs from BALB/c mice at day 5 after tumor inoculation. Data were pooled from three independent experiments (n = 5 mice/experiment).
(G) Experimental design for (H).
(H) Tumor outgrowth of MC38-SIY in *Batf3*$^{-/-}$ mice that were pre-inoculated with MC57-SIY or PBS on the contralateral flank. Numbers in parentheses indicate tumor-free mice. Data were pooled from five independent experiments (n = 2–5 mice/group).
(I) Experimental design for (J).
(J) Tumor outgrowth of MC38-SIY in *Batf3*$^{-/-}$ mice that were pre-inoculated with MC57-SIY-*B2M*$^{-/-}$ or PBS on the contralateral flank. Numbers in parentheses indicate tumor-free mice. Data were pooled from two independent experiments (n = 4 mice/group).
Data are shown as mean ± SEM. *p < 0.05, **p < 0.01: MWU test (B and E).

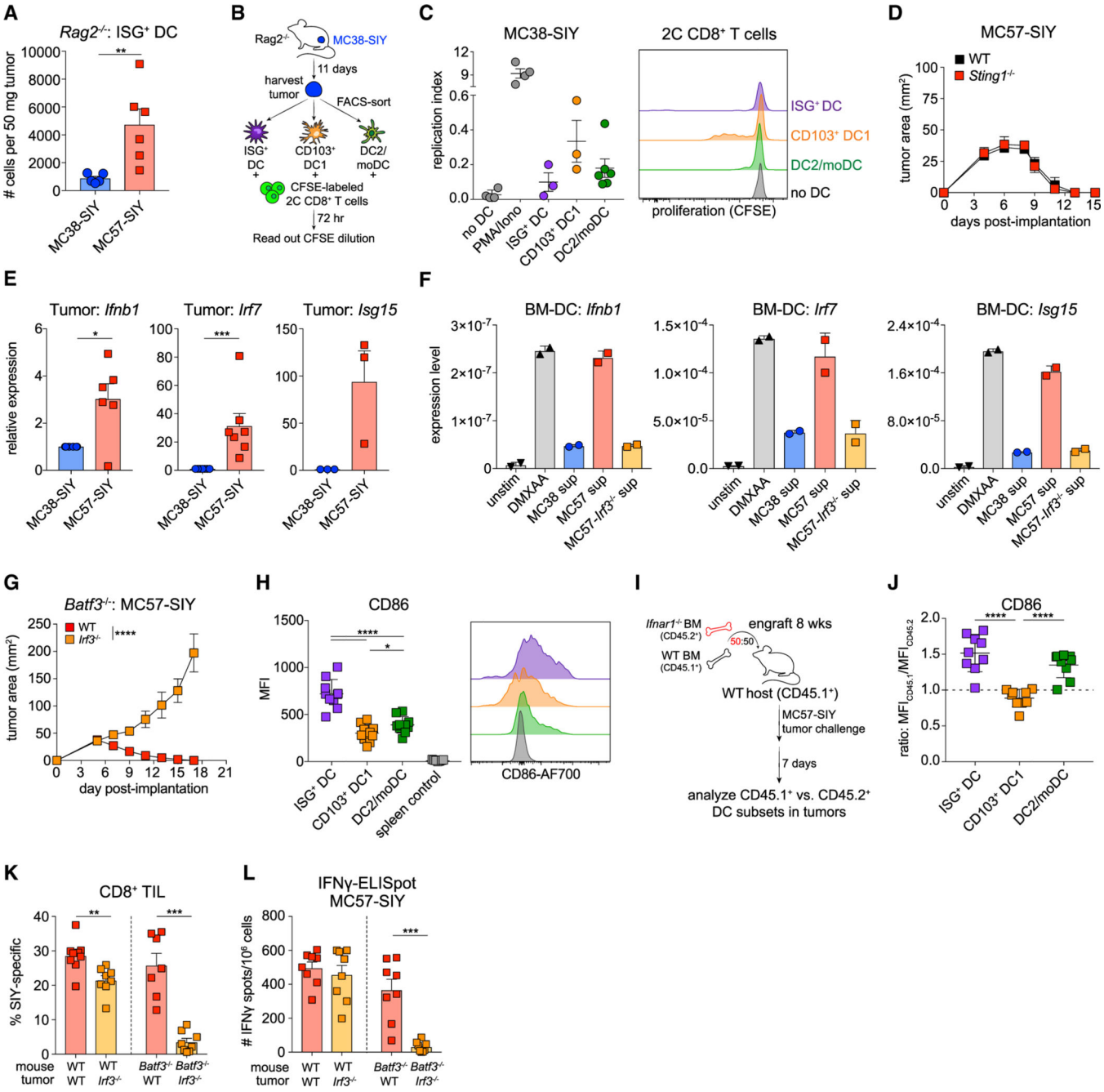

Figure 6. IFNAR signaling in the MC57-SIY TME drives ISG$^+$ DC activation

(A) Number of ISG$^+$ DCs in tumors at day 11 following implantation in *Rag2*$^{-/-}$ mice. Data were pooled from two independent experiments (n = 2–3 mice/group).

(B) Experimental design for (C).

(C) (Left) Replication index of 2C T cells after co-culture with tumor-sorted DCs from *Rag2*$^{-/-}$ mice at day 11 after tumor inoculation. Data were pooled from two independent experiments (n = 5 mice/experiment). (Right) Representative example.

(D) Representative tumor outgrowth (mm^2) in WT or *Sting1*$^{-/-}$ mice (n = 3–5 mice/group; three independent experiments).

(E) Relative expression of *IFNβ1*, *Irf7*, and *Isg15* in tumor cells. Data were pooled from *IFNβ1* (n = 6), *Irf7* (n = 7), and *Isg15* (n = 3) independent experiments.
(F) Expression level of *IFNβ1*, *Irf7*, and *Isg15* in BM-DCs that were unstimulated or cultured with tumor-conditioned media. Data were pooled from two independent experiments.
(G) Representative tumor outgrowth in *Batf3*$^{-/-}$ mice (n = 3–4 mice/group; three independent repeats).
(H) (Left) Geometric mean fluorescence intensity (gMFI) and (right) representative histogram of CD86 expressed by DC subsets from *Rag2*$^{-/-}$ mice at day 11 after tumor implantation (n = 4–5 mice/group; two independent repeats).
(I) Experimental design for (J).
(J) Ratio of the gMFI values of CD86 expressed by CD45.1^{+}:CD45.2^{+} DC subsets. Data were pooled from two independent experiments (n = 5 mice/experiment).
(K and L) Number of SIY-specific TILs (K) and ELISpot quantification of IFN-γ-producing splenocytes (L) from WT and *Batf3*$^{-/-}$ mice at day 7 after tumor implantation. Data were pooled from three independent experiments (n = 3 mice/group).
Data are shown as mean ± SEM. *p < 0.05, **p < 0.01, ***p < 0.001, ****p < 0.0001: MWU test (A, C, E, F, H, and J–L) or two-way ANOVA (D and G).

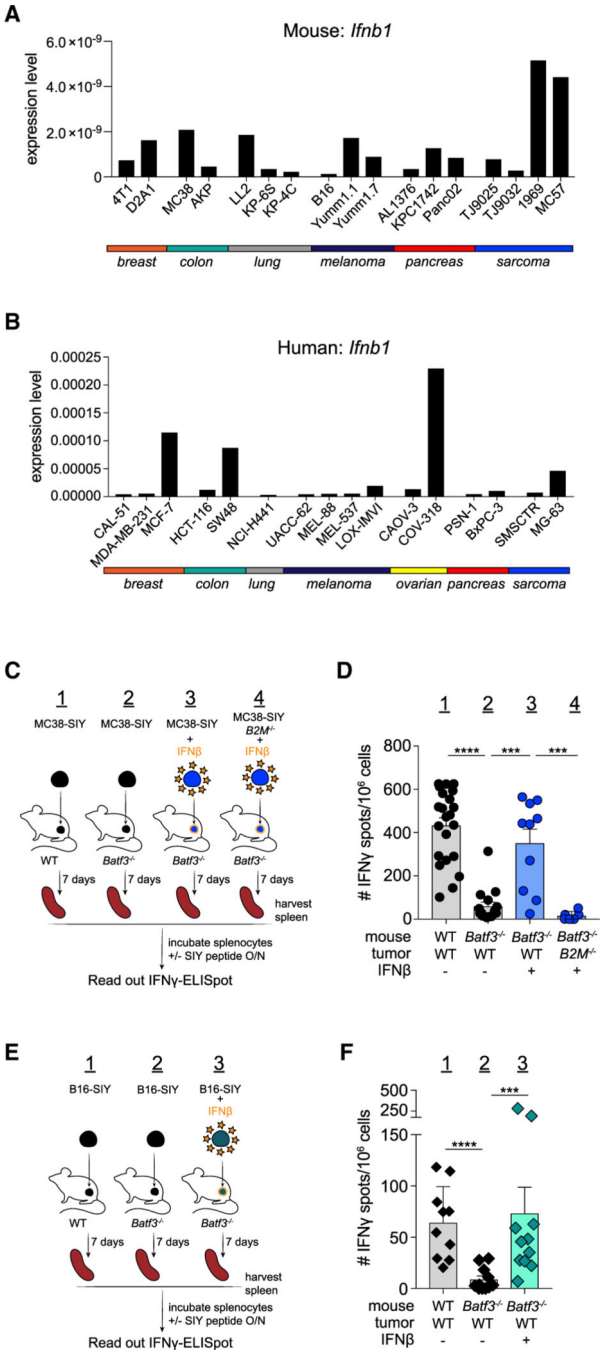

Figure 7. Exogenous addition of IFN-β to progressor tumors restores anti-tumor T cell responses in *Batf3*$^{-/-}$ mice via activation of MHC class I-dressed ISG^{+} DCs

(A and B) Representative expression level of *IFNβ1* in murine (A) and human (B) tumor cell lines (two independent experiments).

(C) Experimental design for (D).

(D) ELISpot quantification of IFN-γ-producing splenocytes from WT and *Batf3*$^{-/-}$ mice at day 7 after tumor implantation. Data were pooled from seven independent experiments (n = 3–5 mice/group).

(E) Experimental design for (F).

(F) ELISpot quantification of IFN-γ-producing splenocytes from WT or *Batf3*$^{-/-}$ mice at day 7 after tumor implantation. Data were pooled from three independent experiments (n = 3–5 mice/group). Data are shown as mean ± SEM. ***p < 0.001, ****p < 0.0001: MWU test (D and F).

Immunity. Author manuscript; available in PMC 2024 January 30.

KEY RESOURCES TABLE

REAGENT or RESOURCE	SOURCE	IDENTIFIER
Antibodies		
anti-mouse AXL (APC); clone MAXL8DS	eBioscience	Cat# 17–1084-82; AB_2734848
anti-mouse AXL (FITC); clone MAXL8DS	eBioscience	Cat# 53–1084-82; AB_2734846
anti-mouse AXL (PE-Cy7); clone MAXL8DS	eBioscience	Cat# 25–1084-82; AB_2734852
anti-mouse β2M; clone EPR21752–214	abcam	Cat# ab218230
anti-mouse CCR7 (PE); clone 4B12	BioLegend	Cat# 120106; AB_389358
anti-mouse c-Kit (FITC); clone 2B8	BioLegend	Cat# 105806; AB_313215
anti-mouse CD103 (APC); clone 2E7	eBioscience	Cat# 17–1031-82; AB_1106992
anti-mouse CD103 (BV711); clone M290	BD Horizon	Cat# 564320; AB_2738743
anti-mouse CD11b (PE-CF594); clone M1/70	BD Horizon	Cat# 562287; AB_11154422
anti-mouse CD11b (PE-Cy7); clone M1/70	BiioLegend	Cat# 101216; AB_312799
anti-mouse CD11c (BV421); clone N418	BioLegend	Cat# 117330; AB_11219593
anti-mouse CD11c (AF488); clone N418	BioLegend	Cat# 117311; AB_389306
anti-mouse CD11c (BUV496); clone N418	BD Optibuild	Cat# 750450; AB_2874611
anti-mouse CD137 (APC); clone 17B5	BioLegend	Cat# 106110; AB_2564297
anti-mouse CD16/32; clone 93	BioLegend	Cat# 101330; AB_2561482
anti-mouse CD16/32 (BV421); clone 93	BioLegend	Cat# 101332,;AB_2650889
anti-mouse CD19 (APC-Cy7); clone 6D5	BioLegend	Cat# 115530; AB_830707
anti-mouse CD24 (BUV737); clone M1/69	BD Horizon	Cat# 565308; AB_2739174
anti-mouse CD24 (BV605); clone M1/69	BioLegend	Cat# 101827; AB_2563464
anti-mouse CD26 (PE); clone H194–112	BioLegend	Cat# 137804; AB_2293047
anti-mouse CD3e (APC-Cy7); clone 17A2	BioLegend	Cat# 100222; AB_2242784
anti-mouse CD3e (BV711); clone 17A2	BioLegend	Cat# 100241; AB_2563945
anti-mouse CD40 (BV711); clone 3/23	BD Optibuild	Cat# 740700; AB_2740384
anti-mouse CD44 (AF700); clone IM7	BioLegend	Cat# 103026; AB_493713
anti-mouse CD45.1 (BUV395); clone A20	BD Horizon	Cat# 565212; AB_2722493
anti-mouse CD45.1 (BV711); clone A20	BioLegend	Cat# 110739; AB_2562605
anti-mouse CD45 (BUV395); clone 30-F11	BD Horizon	Cat# 564279; AB_2651134
anti-mouse CD45 (BV785); clone 30-F11	BioLegend	Cat# 564225; AB_2716861

REAGENT or RESOURCE	SOURCE	IDENTIFIER
anti-mouse CD62L (BV605); clone MEL-14	BioLegend	Cat# 104437; AB_11125577
anti-mouse CD64 (BV711); clone X54–5/7.1	BioLegend	Cat# 139311; AB_2563846
anti-mouse CD64 (BV786); clone X54–5/7.1	BD Optibuild	Cat# 741024; AB_2740644
anti-mouse CD8α (BV711); clone 53–6.7	BioLegend	Cat# 100759; AB_2563510
anti-mouse CD8α (BUV395); clone 53–6.7	BD Horizon	Cat# 563786; AB_2732919
anti-mouse CD80 (PE-Cy7); clone 16–10A1	BioLegend	Cat# 104733; AB_2563112
anti-mouse CD86 (AF700); clone PO3	BioLegend	Cat# 105122; AB_493723
anti-mouse F4/80 (BV785); clone BM8	BioLegend	Cat# 123141; AB_2563667
anti-mouse F4/80 (PE-Cy7); clone BM8	BioLegend	Cat# 123113; AB_893490
anti-mouse F4/80 (APC-Cy7); clone BM8	BioLegend	Cat# 123118; AB_893477
anti-mouse FcεRIα (AF700); clone MAR-1	BioLegend	Cat# 134324; AB_2566734
anti-mouse Flt3 (PE); clone A2F10	BioLegend	Cat# 135306; AB_1877217
anti-human/mouse Granzyme B (AF700); clone QA16A02	BioLegend	Cat# 372222; AB_2728389
anti-mouse H-2K^{b}/H-2D^{b} (FITC); clone 28–8-6	BioLegend	Cat# 114606; AB_313597
anti-mouse H-2K^{b} (PE-Cy7); clone: AF6–88.5	BioLegend	Cat# 116520; AB_2721684
anti-mouse IFNγ (PE-CF594); clone XMG1.2	BioLegend	Cat# 562303; AB_11153140
anti-mouse Lag-3 (BV421); clone C9B7W	BioLegend	Cat# 125221; AB_2572080
anti-mouse Ly6C (AF700); clone HK1.4	BioLegend	Cat# 128023; AB_10640119
anti-mouse Ly6C (APC-Cy7); clone HK1.4	BioLegend	Cat# 128026; AB_10640120
anti-mouse Ly6C (PE); clone HK1.4	BioLegend	Cat# 128007; AB_1186133
anti-mouse MHCII (AF700); clone M5/114.15.2	eBioscience	Cat# 56–5321-80; AB_494009
anti-mouse MHCII (BUV805); clone M5/114.15.2	BD Optibuild	Cat# 748844; AB_2873247
anti-mouse MHCII (BV510); clone M5/114.15.2	BioLegend	Cat# 107636; AB_2734168
anti-mouse NK1.1 (APC-Cy7); clone PK136	BioLegend	Cat# 108724; AB_830871
anti-mouse PD-1 (PE-Cy7); clone RMP1–30	BioLegend	Cat# 109110; AB_572017
anti-mouse Sca-1 (BV785); clone D7	BioLegend	Cat# 108139; AB_2565957
anti-mouse Siglec-H (BUV661); clone 440c	BBD Optibuild	Cat# 749806; AB_2874060
anti-mouse SIINFEKL/H-2Kb (biotinylated); clone 25-D1.16	eBioscience	Cat# 13–5743-81; AB_1210600
anti-mouse Sirpα (AF488); clone P84	BioLegend	Cat# 144024; AB_2650815
mouse IgG1κ isotype control (biotinylated); clone P3.6.2.8.1	eBioscience	Cat# 13–4714-85; AB_470089
recombinant human Flt3L-Ig; clone Flt-3L-Ig (hum./hum.)	Bio X Cell	Cat# BE0098; AB_10949072

REAGENT or RESOURCE	SOURCE	IDENTIFIER
anti-mouse NK1.1; clone PK136	Bio X Cell	Cat# BP0036; AB_1107737
mouse IgG2a isotype control; clone C1.18.4	Bio X Cell	Cat# BP0085; AB_1107771
anti-mouse CD8; clone 2.43	Bio X Cell	Cat# BE0061; AB_1125541
anti-mouse CD4; clone GK1.5	Bio X Cell	Cat# BE0003; AB_1107636
Chemicals, peptides, and recombinant proteins		
SIY-pentamer (PE)	ProImmune	Cat# F1803–2B-D
streptavidin (BV711)	BioLegend	Cat# 405241
fixable viability eFluor780	eBioscience	Cat# 65–0865-18
fixable viability eFluor506	eBioscience	Cat# 65–0866-14
recombinant murine IFNβ	Dane Wittrup Lab (MIT)	N/A
Liberase TL Research Grade	Sigma-Aldrich	Cat# 05401020001
DNase I, Grade II, from bovine pancreas	Sigma-Aldrich	Cat#10104159001
Phorbol 12-myristate 13-acetate	Sigma-Aldrich	Cat# P8139
Ionomycin from Streptomyces conglobatus	Sigma-Aldrich	Cat# I9657
Diphtheria Toxin from Corynebacterium	Sigma-Aldrich	Cat# D0564
SIYRGGYL peptide	Thomas Gajewski Lab (UChicago)	N/A
DMXAA murine STING ligand	Invivogen	Cat#tlrl-dmx
TRIzol Reagent	Thermo Fisher Scientific	Cat# 15596026
Critical commercial assays		
IFNγ-ELISpot Set	BD Biosciences	Cat# 551083
CellTrace CFSE Cell Proliferation Kit	Thermo Fisher Scientific	Cat# C34554
CellTrace Violet Cell Proliferation Kit	Thermo Fisher Scientific	Cat# C34571
AEC Substrate Set	BD Biosciences	Cat# 551951
High Capacity cDNA Reverse Transcription Kit	Thermo Fisher Scientific	Cat# 43–488-13
RNase-Free DNase Set	QIAGEN	Cat# 79254
RNeasy Mini Kit	QIAGEN	Cat# 74106
RNeasy MinElute Cleanup Kit	QIAGEN	Cat# 74204
Quick-RNA MicroPrep Kit with Zymo-Spin IC Columns	Zymo Research	Cat# R1051
In-Fusion HD Cloning Plus	Takara Bio	Cat# 639645

REAGENT or RESOURCE	SOURCE	IDENTIFIER
Precision Count Beads	BioLegend	Cat# 424902
UltraComp eBeads Compensation Beads	Thermo Fisher Scientific	Cat# 01–2222-42
FoxP3 Transcription Factor Staining Buffer Kit	Thermo Fisher Scientific	Cat# 00–5523-00
Deposited data		
Murine scRNA-seq data ($CD45^+$ cells in MC57-SIY tumors)	This paper	GSE181939
Murine bulk RNA-seq data (sorted WT and $Rag2^{-/-}$ DC subsets)	This paper	GSE181939
Experimental models: Cell lines		
MC57 parental	Thomas Gajewski Lab (UChicago)	N/A
MC57-SIY-GFP	Thomas Gajewski Lab (UChicago)	N/A
MC57-SIY-GFP-$\beta2M^{-/-}$	This paper	N/A
MC57-SIY-GFP-$IRF3^{-/-}$	This paper	N/A
MC57-cerulean-SIIN-SIY	This paper	N/A
MC38 parental	Thomas Gajewski Lab (UChicago)	N/A
MC38-SIY-GFP	Thomas Gajewski Lab (UChicago)	N/A
MC38-SIY-GFP-$\beta2M^{-/-}$	This paper	N/A
1969-SIY-GFP	Thomas Gajewski Lab (UChicago)	N/A
B16-SIY-dsRed	Thomas Gajewski Lab (UChicago)	N/A
Please refer to Table S6 for cell lines used in mouse/human *Ifnb1* qPCR screens.		N/A
Experimental models: Organisms/strains		
Mouse: C57BL/6	Taconic	Stock# B6-F
Mouse: BALB/c	Taconic	Stock# BALB-F
Mouse: $Rag2^{-/-}$	Taconic	Stock# RAGN12-F
Mouse: $Batf3^{-/-}$	Jackson Laboratory	Stock# 013755
Mouse: $\beta2M^{-/-}$	Jackson Laboratory	Stock# 002087
Mouse: $CD11c^{Cre}$	Jackson Laboratory	Stock# 008068
Mouse: CD11c-DTR	Jackson Laboratory	Stock# 004509
Mouse: $Clec9a^{-/-}$	Jackson Laboratory	Stock# 017696

REAGENT or RESOURCE	SOURCE	IDENTIFIER
Mouse: Ifnar1$^{-/-}$	Jackson Laboratory	Stock# 028288
Mouse: Irf4$^{f/f}$	Jackson Laboratory	Stock# 009380
Mouse: 2C Rag2$^{-/-}$ TCR-transgenic	Thomas Gajewski Lab (UChicago)	N/A
Mouse: OTI TCR-transgenic	Jackson Laboratory	Stock# 003831
Mouse: zDC-DTR	Jason Cyster (UCSF) and Thorsten Mempel (Harvard/MGH)	Meredith et al., 2012
Oligonucleotides		
Please refer to Table S5.		N/A
Recombinant DNA		
Plasmid: pLV-EF1α-IRES-puro	Addgene	Cat# 85132
Plasmid: Cerulean-N1	Addgene	Cat# 54742
Plasmid: px459-Cas9-puro	Addgene	Cat# 62988
Software and algorithms		
FlowJo v10.5.3	TreeStar	https://www.flowjo.com
GraphPad Prism v7	GraphPad	https://www.graphpad.com
Adobe Illustrator CC2018	Adobe	https://www.adobe.com
Seurat v3.2.2	Rahul Satija Lab (NYU)	https://www.satijalab.org/seurat/
10X Genomics Cell Ranger v3.0.1	10X Genomics	https://www.10xgenomics.com
Bowtie v1.2		http://bowtie-bio.sourceforge.net/bowtie2/index.shtml
RSEM v1.3.1		https://bmcbioinformatics.biomedcentral.com/articles/10.1186/1471–2105-12–323
DESeq2 v1.26.0		https://genomebiology.biomedcentral.com/articles/10.1186/s13059–014-0550–8
GSEA v4.1.0		https://www.gsea-msigdb.org/gsea/index.jsp